Journal of Materials Research and Technology 29 (2024) 2554–2571

Contents lists available at ScienceDirect

Journal of Materials Research and Technology

journal homepage: www.elsevier.com/locate/jmrt

Optimizing magnetic performance of Fe–50Ni alloy for electric motor cores through LPBF: A study of as-built and heat-treated scenarios

M. Ahmadnia [a,*], E. Fereiduni [a], M. Yakout [b], M. Elbestawi [a], R.K. R M [c], G. Vakil [c], R. Muizelaar [d]

[a] *Department of Mechanical Engineering, McMaster University, Hamilton, ON, Canada*
[b] *Department of Mechanical Engineering, University of Alberta, Edmonton, AB, Canada*
[c] *Electrical & Electronic Engineering, University of Nottingham Faculty of Engineering, Nottingham, UK*
[d] *Stackpole International, 2400 Royal Windsor Drive, Mississauga, ON, Canada*

ARTICLE INFO

Keywords:
Soft magnetic materials
Laser powder bed fusion (LPBF)
Electric motor (EM)
Texture
Coercivity
Eddy-current loss

ABSTRACT

This study aims to identify the optimal combination of process variables for laser powder bed fusion (LPBF) of electric motor (EM) cores using Fe–50Ni alloy. A thorough analysis of mechanical and magnetic properties, with a focus on its dynamic magnetic performance within 50–500 Hz frequency range, is presented. Optimized process parameters yielded relative densities above 99%. In the as-built condition, high hardness (twice that of conventionally processed alloy) and high ductility (>30% at rupture) were achieved. The as-built samples demonstrated magnetic properties below the requirements, but significant improvement was observed in the semi-static magnetic properties after heat treatment, with acceptable coercivity (44 A/m) and maximum permeability ($\sim 10^4$) attributed to a notable reduction in geometrically necessary dislocations (GNDs) density. Heat treatment did not significantly reduce the total loss at high flux densities or elevated testing frequencies because the energy loss in the as-built microstructure is lower than what is expected due to the activation of more domain walls resulting in a homogeneous distribution of eddy currents. The superior semi-static performance of the optimum sample is related to its texture, which was more oriented toward the easy axis of magnetization in this alloy (<111> direction). This research demonstrates the LPBF process's potential for manufacturing electric motor soft cores, providing acceptable surface integrity, roughness levels, and desired coercivity and permeability. However, the high total loss, specifically at elevated frequencies, highlights the need for additional capabilities of LPBF, such as fabricating multi-materials, to mitigate energy losses without resorting solely to heat treatment.

1. Introduction

The increasing shift towards a more electrified world underscores the importance of achieving a more efficient conversion of electrical energy to mechanical energy, a process primarily carried out by electric motors (EMs). Industries are fervently pursuing lightweight machines with enhanced efficiency [1]. However, the current state of electrical machinery and manufacturing technology is inadequate to meet these demands. Reducing the cost of design modifications and assembly processes necessitates the implementation of part count reduction methods, which are unattainable through traditional manufacturing approaches.

Additive Manufacturing (AM) emerges as a potential solution, as it offers benefits in terms of reducing the number of components in assemblies and enabling automated manufacturing processes. AM utilizes a layer-by-layer material addition technique to fabricate the required parts, thereby facilitating the production of parts with complex geometries or the consolidation of multiple components to streamline complexity [2,3]. Additionally, the inherent layer-wise nature of AM presents an opportunity to manufacture electric EM cores with lower eddy-current loss. By employing thinner layers compared to the conventional stacking of laminations used in shaping EM rotors and stators, AM provides a pathway to mitigate eddy-current losses.

Extensive research has been conducted to explore the production of soft magnetic components for EMs using various AM technologies [4–11]. Among these technologies, the most commonly practiced method for metal processing is the laser powder bed fusion (LPBF) process, also referred to as selective laser melting. In this process, a fine

---

* Corresponding author.
E-mail address: Ahmadnim@mcmaster.ca (M. Ahmadnia).

https://doi.org/10.1016/j.jmrt.2024.02.011
Received 3 August 2023; Received in revised form 25 January 2024; Accepted 2 February 2024
Available online 5 February 2024

metal powder layer is uniformly deposited on a build plate through a coating mechanism. Subsequently, each layer is selectively melted using a high-power laser beam, resulting in the fusion of a 2D slice that conforms to the desired part shape [12].

Soft magnetic materials, which serve as the core of electric motors and generators, possess specific characteristics, including a narrow hysteresis loop (low coercivity), high saturation magnetization, and high permeability (10^3 times greater than vacuum permeability) [13]. Additionally, these materials need to exhibit low energy loss (high efficiency) when operating at high frequencies. The total energy loss in a magnetic core comprises hysteresis loss, eddy-current loss, and excess loss [14]. While hysteresis loss is directly proportional to the material's coercivity, the other types of losses depend on factors such as magnetic flux density, electric conductivity, laminate thickness, and material microstructure [14,15].

Using the LPBF process, various soft magnetic materials, including Fe, Fe–Si, Fe–Ni, Fe–Co, and amorphous components, have been successfully fabricated. Specifically, water-atomized pure Fe [16,17], and Fe–Si alloy [18–20] have been extensively investigated concerning their mechanical properties and magnetic performance. However, it is worth noting that high-Si steel alloys, despite their advantages in electric machine applications due to their high saturation magnetization and relatively lower costs, are prone to crack formation during the rapid solidification process, making the measurement of their magnetic performance unfeasible [20].

Ni–Fe alloys, commonly known as permalloys, constitute another sub-category of soft magnetic alloys. Although these alloys exhibit lower saturation magnetization compared to Si steels and Fe–Co alloys, they are well-suited for small high-speed machines due to their exceptionally low magnetic coercivity and reduced core loss at low working frequencies [21]. Additionally, permalloys possess remarkably higher relative permeability [22].

A limited number of researchers have explored the processing of permalloy powders using either LPBF or direct energy deposition (DED) processes. The magnetic properties of the fabricated parts are comparable to or even superior to those produced through conventional methods [9,20,23–28], except for coercivity, which is likely attributed to defects induced during the manufacturing process [9,10]. Higher coercivity translates to increased hysteresis loss and negatively impacts the maximum relative permeability of these alloys. Consequently, it is crucial to reduce porosity and microstructural defects in printed parts. This can be achieved by controlling process variables such as laser power and scanning speed, which directly influence the cooling rate and exposure time of the melt pool [29]. Other process parameters, such as hatch spacing and the number of scan passes, have been reported to have minimal significance [30]. Furthermore, appropriate heat treatment strategies have been shown to reduce coercivity while also mitigating the material's hardness, as demonstrated by Mazeeva et al. in their study of the Fe–50Ni alloy [31].

The typical Ni–Fe alloys utilized in EMs contain approximately 40–50% Ni, as this composition maximizes the saturation magnetization, particularly when the Ni content is around 48% [32]. This alloy has gained attention for LPBF processing, as it possesses an intrinsic ductile microstructure, allowing for the creation of integral crack-free structures, unlike high-Si steels. To implement the LPBF process effectively for this alloy, it is crucial to identify the appropriate process parameter window that yields low porosity, minimal surface roughness, and sound mechanical properties.

While more than 130 process variables have been identified to affect the final properties of LPBF-fabricated parts [33], several key parameters significantly influence the outcome, including laser power, scanning speed, hatch spacing, and layer thickness [34]. Conducting comprehensive parametric studies to investigate all these variables can be extensive and complex. As a result, researchers have agreed to utilize volumetric energy density (VED) or absorbed energy density (AED) [35] as the predictors of relative density and descriptors of experimental data. These parameters are formulated based on the most influential process variables, as follows:

$$VED = \frac{P}{vht} \tag{1}$$

$$AED = \frac{\beta}{h\sqrt{4\alpha\varnothing}}\frac{P}{\sqrt{v}} \tag{2}$$

Where $\boldsymbol{P}$ is the laser power (W), $\boldsymbol{v}$ is the scanning speed (mm/s), $\boldsymbol{h}$ is the hatch spacing (mm), $\boldsymbol{t}$ is the powder layer thickness (mm), $\boldsymbol{\beta}$ is the laser absorptivity of powder, $\varnothing$ is the laser beam diameter (mm), and $\boldsymbol{\alpha}$ considers the material properties as thermal diffusivity (mm^2/s). The impact of *VED* has been extensively studied regarding its influence on various properties of fabricated parts, with a limited number of studies investigating the relationship between *VED* and properties of samples fabricated from Ni-containing alloys [36,37], as well as soft magnetic Fe–Ni alloys [9,23,27]. However, the existing research on Fe–Ni alloys has primarily focused on examining the effects of individual parameter variations on relative density, hardness, or magnetic properties under DC magnetic fields. Considering the specific application of the Fe–50Ni alloy as EM cores, there is a lack of comprehensive studies evaluating the influence of process parameters on the structure, mechanical properties, and magnetic properties. Notably, investigations on the dynamic performance of this alloy, processed using PBF techniques under an AC magnetic field, remain unreported, and the magnetic efficiency of this alloy when processed by LPBF, as well as the potential influence of process variables on the total energy loss, have yet to be assessed and compared to those of traditionally manufactured cores.

The objective of this study is to comprehensively analyze the impact of various process parameters on the physical and mechanical properties of the Fe–50Ni alloy. Additionally, the dynamic magnetic performance of the alloy under different working frequencies, up to 500 Hz, corresponding to the speed of the associated electric rotor, is investigated using the LPBF process. The ultimate goal is to determine the optimal combination of process variables that can yield parts fabricated from the Fe–50Ni alloy with the highest mechanical properties and optimal magnetic performance in a soft magnetic regime. The magnetic performance of the fabricated parts is evaluated under both DC and AC magnetic fields. Additionally, the microstructural parameters governing the total loss of the alloy in both as-built and heat-treated conditions are explored and discussed.

2. Materials and methods

2.1. Feedstock

The powder used in this study was a gas-atomized Fe–50%Ni powder (Fe-49.3Ni-0.19Mn-0.07Si wt%), supplied by Sandvik Osprey LTD., UK. Particle size distribution analysis was conducted on this powder using a Malvern Mastersizer 3000 equipped with a Hydro LV module and employing water as the dispersant. The powder's D_{10}, D_{50}, and D_{90} were 26.1, 36.9, and 51.7 μm, respectively.

2.2. Process optimization, sample production, and heat treatment

The samples were fabricated using an EOS M280 LPBF machine (EOS, Krailling, Germany), which was equipped with a Yb-fiber laser system capable of delivering power levels up to 400 W. The fabrication process was carried out under a nitrogen atmosphere to ensure that the oxygen content in the chamber remained below 0.13%. The experimental procedure in this study was conducted in two stages. A full factorial design of experiments was employed to investigate the impact of three process parameters, namely laser power (P), scanning speed (V), and hatch spacing (H). The evaluation focused on various properties, including relative density (RD), residual stresses (RS), surface roughness, and microstructural defects. Other process parameters, such as build platform pre-heating (40 °C), stripe width (100 mm), hatch rotation angle (67^{o}), and layer thickness (40 μm), were kept constant across all samples. Each combination of process parameters, denoted as P_V_H, was used to fabricate three cubic-shaped coupons with a side length of 8 mm. This resulted in a total of 81 cubes (3 × 3ˆ3) being allocated on the build plate, as outlined in Table 1. Four sets of process parameters yielding the most desirable properties were selected from this build. The criteria for their selection were based on high relative density (see Table 3) and relatively smooth surface roughness compared to other coupons (see Table 3). These samples were labeled as P (240_750_0.08), Q (240_750_0.10), S (330_750_0.08), and T (330_750_0.10) and two ring-shaped samples, following the dimensions specified in IEC60404-4 [38], for examining the magnetic properties were fabricated. A block with dimensions of 10 mm (width) × 10 mm (height) × 110 mm (length) was fabricated using the same parameters as sample Q, and three tensile samples, adhering to ASTM E8 requirements [39], were sliced from the block using wire-electric discharge machining (EDM). The build plate used was made of MS1 grade maraging steel, and the cubes, blocks, and toroids were cut from it using wire EDM. Heat treatment of the cubes and toroids was conducted in a chamber with a protective atmosphere consisting of 95% Ar and 5% dry hydrogen, with a flow rate of 100 SCC/min. The samples were heated up to 1200 °C, then cooled down to room temperature at a heating and cooling rate of 2.5 °C/min. The dwell time at the target temperature was 6 h for all samples. A schematic illustration of the steps involved in this work can be seen in Fig. 1.

2.3. Microstructural, mechanical, and material characterization

The densification level of printed coupons was assessed at room temperature using the Archimedes method in accordance with the ASTM B962-14 standard. The bulk density of disordered Fe–50Ni alloy was regarded as 8.22 g/cm^3 [41]. The surface roughness of the coupons was measured using a Mitutoyo SJ-410 stylus profilometer. The arithmetic mean deviation (Ra) of both the top and side surfaces was measured and documented. The stylus movement direction was perpendicular to the scan lines on the top surfaces, while on the side walls, measurements were conducted parallel to the build direction. The cut-off length was set at 0.8 mm, resulting in measurements being performed over an evaluation length of 4.0 mm [42].

For hardness testing, a CLEMEX CMT. HD manual microhardness tester with a Vickers indenter was employed. The tests were conducted at three different heights (1, 3, and 5 mm from the bottom of the cubes, as shown in Fig. 2) on a plane parallel to the building directions (YZ-plane). Three indents were made at each level, and the average of nine measurements were reported. The applied load was 300 gf with a dwell time of 10 s.

The surface of the coupons, as well as non-etched sections, were observed using a Keyence VHX digital microscope to qualitatively compare the densification of samples. After polishing the sections with colloidal silica (average particle diameter of 0.04 μm), Kalling's reagent (No.2) was used to reveal the microstructure.

Electron backscatter diffraction (EBSD) analysis was employed to characterize the texture, grain size and morphology, and dislocation density on the YZ-section of samples (see Fig. 2). This analysis utilized an FEI Versa 3D field-emission scanning electron microscope (FE-SEM) with an accelerating voltage of 20 keV and a tilt angle of 70°, using a step size of 0.7 μm. The EBSD data were collected using TSL OIM 7 software and analyzed using the AZtecCrystal EBSD processing software package.

Phase analysis and surface residual stress measurements were conducted using a Co Kα radiation source with a wavelength of 1.79206 Å and a 1-mm collimator. For residual stress measurements, a 2θ angle of 111.662° corresponding to a lattice plane of 3 1 1 was employed. A total of 24 frames were acquired, consisting of 6 Phi angles (0°, 60°, 120°, 180°, 240°, and 300°) and 4 Phi angles (6°, 19.3°, 32.7°, 46°). The anisotropy factor (Ar_x) of the material, considered as a nickel-based alloy, was set to 1.52 [43]. Residual stress measurements were taken on the top surface of the samples to obtain the residual stresses in-plane perpendicular to the building direction.

2.4. Evaluation of magnetic properties

The surface finish of the printed toroids was achieved by grinding both the top and bottom surfaces. The height of the samples was maintained at 4.5 ± 0.01 mm for all specimens. To determine the DC hysteresis loop, measurements were conducted in accordance with the relevant standard [38]. The primary winding current and secondary winding voltage were measured to calculate the inducting magnetic field (H) and magnetic flux density (B), respectively. Under static conditions, the magnetic performance of the samples was evaluated based on several parameters. These include the maximum relative permeability ($\boldsymbol{\mu_{max}}$), relative permeability at an applied field strength of 40 A/m ($\boldsymbol{\mu_{40}}$), flux density at applied field strengths of 5 kA/m and 10 kA/m (referred to as $\mathbf{B_{50}}$ and $\mathbf{B_{100}}$, respectively), and the coercivity extracted from the B–H curve. The dynamic magnetic performance of the toroids was assessed following the guidelines outlined in Ref. [44]. The common watt-meter method was employed to measure the losses. Total power losses were reported at excitation frequencies of 50, 200, 400, and 500 Hz, at output flux densities of B = 0.5 and B = 1 T. The measurements were repeated to achieve a level of uncertainty equal to or less than 3%.

3. Results and discussion

3.1. Manufacturing quality and defects

3.1.1. Relative density

Fig. 3 depicts the relative density of samples versus implemented laser power, scanning speed, and hatch spacing. Comparing the results, it is clear that in the range of process variables employed in this study, the scanning speed was the most significant parameter as the majority of coupons with the highest level of densification were obtained when the scanning speed was 750 mm/s. At a relatively low scanning speed, the

Table 1
The process parameters used in the first stage of this study to fabricate samples (DOE matrix of the full factorial design).

Name	Power (w)	V (mm/s)	h (mm)	VED (J/mm^3)	Name	Power (w)	V (mm/s)	h (mm)	VED (J/mm^3)	Name	Power (w)	V (mm/s)	h (mm)	VED (J/mm^3)
K	150	300	0.08	156.3	**M**	150	750	0.08	62.5*	**II**	150	1200	0.08	39.1
J	150	300	0.1	125	**N**	150	750	0.1	50**	**G**	150	1200	0.1	31.3
L	150	300	0.12	104.2	**O**	150	750	0.12	41.7^{+}	**F**	150	1200	0.12	26
C	240	300	0.08	250	**P**	240	750	0.08	100	**V**	240	1200	0.08	62.5*
E	240	300	0.1	200	**Q**	240	750	0.1	80	**W**	240	1200	0.1	50**
H	240	300	0.12	166.7	**R**	240	750	0.12	66.7	**I**	240	1200	0.12	41.7^{+}
A	330	300	0.08	343.8	**S**	330	750	0.08	137.5	**X**	330	1200	0.08	85.9
B	330	300	0.1	275	**T**	330	750	0.1	110	**Y**	330	1200	0.1	68.8
D	330	300	0.12	229.2	**U**	330	750	0.12	91.7	**Z**	330	1200	0.12	57.3

*, **, + Combinations with the same VED.

Table 2
Classification of top and side surface roughness of coupons based on the criteria introduced in Ref. [40].

Sample Name	Surface Roughness Class		Sample Name	Surface Roughness Class		Sample Name	Surface Roughness Class	
	Top	**Side**		**Top**	**Side**		**Top**	**Side**
K	N9	N9	**M**	N9	N9	**II**	N10	N9
J	N10	N9	**N**	N9	N10	**G**	N10	N10
L	N10	N9	**O**	N10	N10	**F**	N10	N10
C	N8	N9	**P**	N8	N9	**V**	N9	N9
E	N9	N9	**Q**	N8	N9	**W**	N9	N9
H	N9	N9	**R**	N9	N9	**I**	N10	N10
A	N8	N10	**S**	N8	N10	**X**	N9	N9
B	N8	N10	**T**	N8	N9	**Y**	N10	N9
D	N9	N10	**U**	N9	N10	**Z**	N10	N10

Table 3
Properties of six samples with the highest relative densities primarily selected for further characterizations in this work.

Name	Power (w)	V (mm/s)	h (mm)	VED (J/mm^3)	RD (%)	Top Surface Roughness (based on Ra in um) [40]	Hardness (HV$_{0.3}$)	
V	240	1200	0.08	62.5	98.62 ± 0.60	N9	181.3 ± 4.6	Not Selected
R	240	750	0.12	66.7	98.55 ± 0.52	N9	181.1 ± 3.1	Not Selected
Q	240	750	0.10	80	99.17 ± 0.15	N8	181.9 ± 6.1	Selected
P	240	750	0.08	100	98.98 ± 0.50	N8	179.2 ± 2.9	Selected
T	330	750	0.10	110	98.73 ± 0.41	N8	179.3 ± 4.8	Selected
S	330	750	0.08	137.5	98.69 ± 0.28	N8	174.1 ± 6.1	Selected

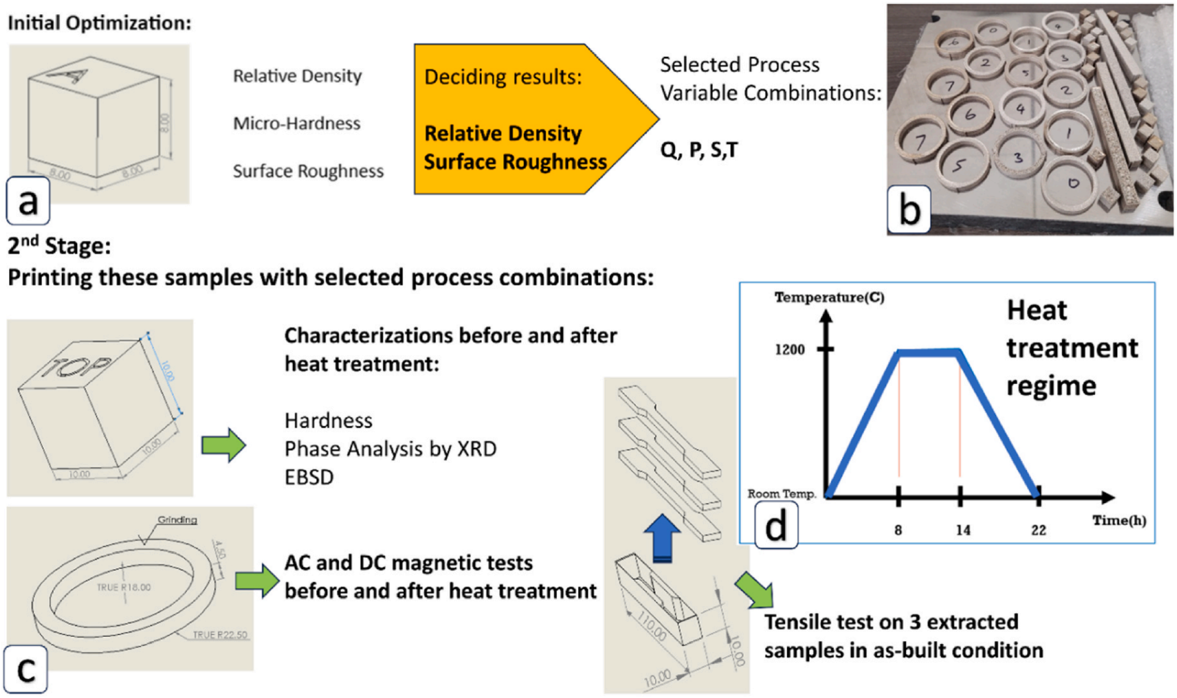

Fig. 1. Schematic illustration of the workflow in this research: (a) schematic design of coupons printed in the first stage and characterization methods employed to find the optimum set of process variables. Based on the results of relative density and surface roughness, four different sets of process parameters were selected for the second stage. (b) Three coupons, two toroids, and one block printed for each selected set of process parameters. (c) Dimensions of designed coupons, toroids, and blocks printed in the second build as well the schematic illustration of three tensile samples extracted from the printed blocks using Wire-EDM. (d) Heat-treatment procedure implemented on coupons and toroids, depicting corresponding heat and cooling ramps and dwell time.

RD was comparably low, and further explorations revealed that numerous spherical pores caused by the keyhole effect were the reason behind the decreased density. When the scanning speed increased to 750 mm/s, the keyhole-induced porosities mainly vanished, and RD increased. At relatively high scanning speeds, the densification level deteriorated again due to the insufficient energy and the associated lack of fusion (LoF) defects generated with the sample (see Fig. 4(b)).

Concerning laser power, it is observed that at relatively low scanning

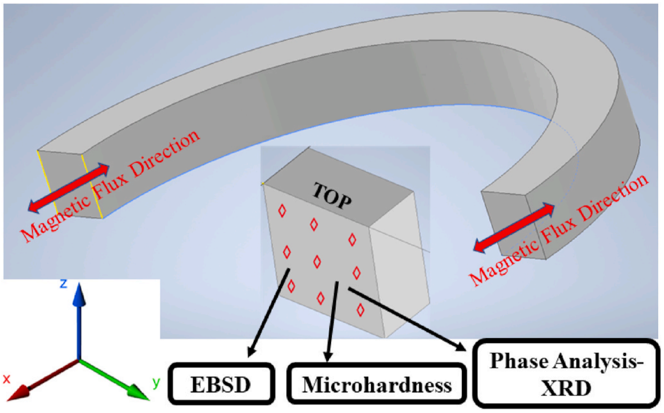

Fig. 2. The vertical section (parallel to build direction-Z axis) of toroids and the corresponding section of cubes which were used to perform EBSD, XRD, and microhardness tests. The red diamonds drawn on the vertical section of the cube represent the loci of micro-hardness indents. The XRD and EBSD analysis was also conducted on the vertical section.

speeds, the RD decreased by increasing the laser power, regardless of the hatch spacing employed. This is believed to be caused by more keyhole porosities formed at relatively low scanning speeds. At relatively high scanning speeds, on the other hand, higher laser powders promoted higher densities by reducing LoF-induced defects.

Among the three process parameters studied here, results showed that hatch spacing was the least significant variable affecting RD; however, its effect was more evident at relatively high scanning speeds (v = 1200 mm/s). Nonetheless, some patterns could be detected through careful consideration of the results depicted in Fig. 3. As shown in Fig. 5, elevation of hatch spacing led to an increase in RD for the three samples printed using the same laser power and scanning speed but different hatch spacings (samples K, J, and L). This originates from more pronounced keyhole porosities induced by elevated energy densities when decreasing the hatch spacing.

The relative density and hardness of samples versus the VED is shown in Fig. 6. The obtained relative density of the coupons ranges from 90.3% to 99.1%. In this study, samples with densities equal to or above 98.5% were considered highly dense. As per the relative density measurement results, samples V, R, Q, P, T, and S met the minimum relative density required, spanning in the VED range of 70–140 J/mm^3. At VED values below and above this optimum range, the densification level was jeopardized through the irregular-shaped lack of fusion porosities and spherical keyhole porosities, as also extensively reported in the literature [45,46]. It is worth noting that not all samples lying within the optimum VED range possessed relative densities above 98.5%, signifying the limitations associated with using Eq. (1) to accurately predict the density of the fabricated parts. For instance, the VED of samples L and J (marked on Fig. 6) are equal to 104 and 125 J/mm^3 which fall within the optimum range reported above, but their corresponding RD are far below 98.5% due to insufficient deposited energy to provide good fusion (low laser power with hatch spacing equal to 0.12 and 0.10 mm, respectively). Therefore, the optimum VED range proposed in this study should be used with caution and complemented with experimental validation upon using different combinations of process parameters yielding VED values in this range.

3.1.2. Hardness

Fig. 6 also shows the variation in microhardness of samples against their VED, while Fig. 7 depicts the microhardness values in relation with the process parameters employed. The average hardness of all samples varies between 145 and 180 HV$_{0.3}$. These values are far above the hardness reported for annealed alloy (~90 Hv [47]) and just above the alloy with similar composition processed by LENS (~140 HV [7]). Referring to Fig. 7, a monotonous trend between process variables and resultant hardness could not be easily drawn. For example, while at high scanning speeds, elevating the laser power leads to higher hardness (Fig. 7(c)), a decreasing trend is the case at low scanning speed (Fig. 7 (a)). Moreover, decreasing the hatch spacing at high scanning speeds improves the hardness (Fig. 7(c)), but the same trend could not be seen

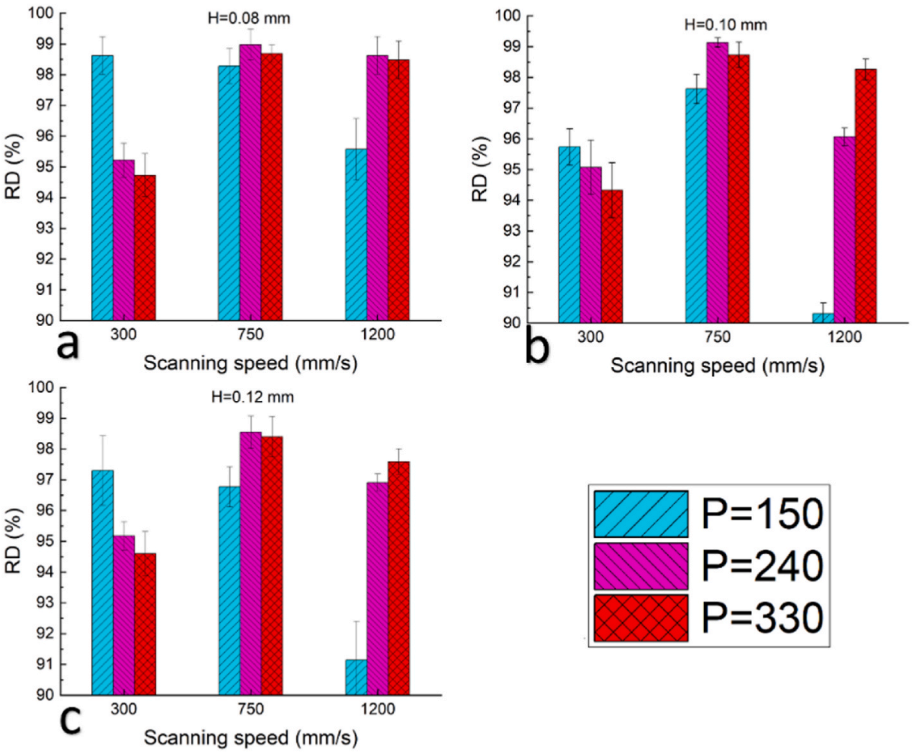

Fig. 3. Average relative density of samples printed using different scanning speeds and laser powers at a hatch spacing of: (a) 0.08, (b) 0.10, and (c) 0.12 mm.

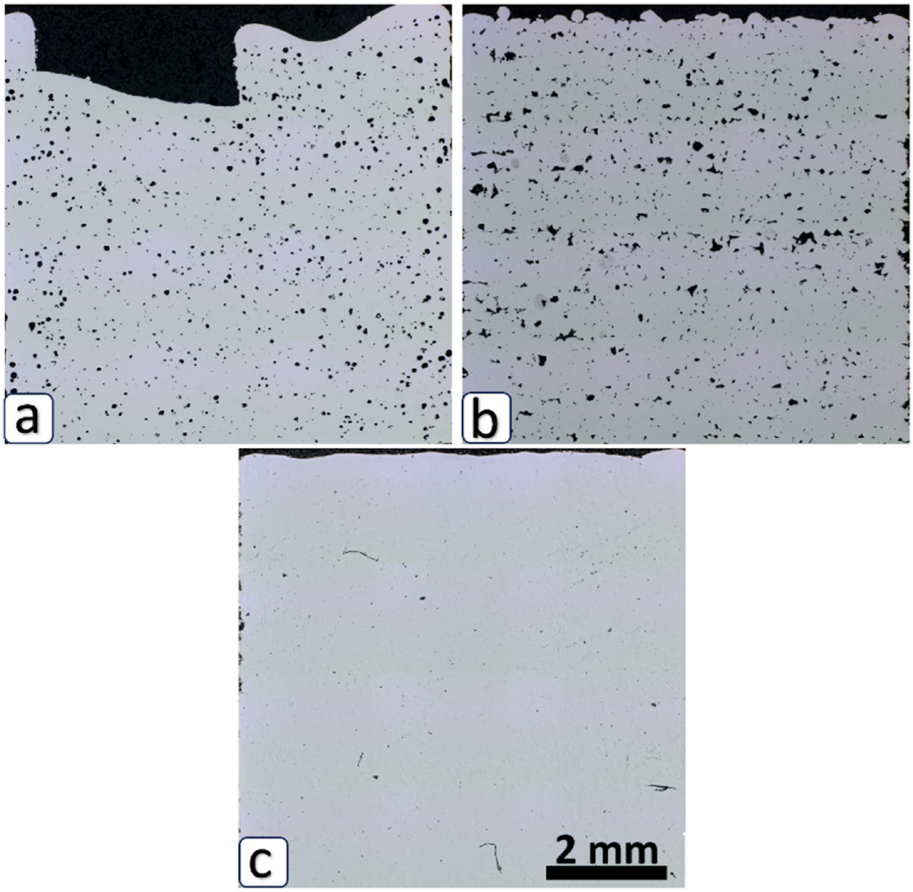

Fig. 4. Optical micrographs showing the effect of scanning speed on part quality when laser power is 240 W and hatch spacing is 0.12 mm. (a) V = 300 mm/s (spherical shape porosities are dominant), (b) V = 1200 mm/s (LoF is the major reason for porosity), and (c) V = 750 mm/s (sample with the high densification level is achieved).

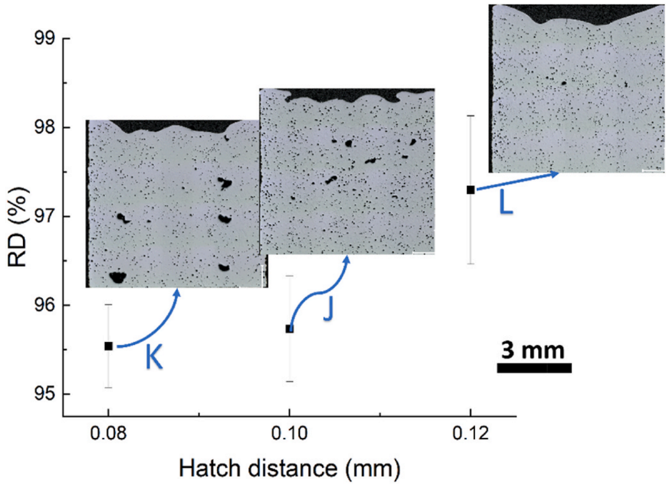

Fig. 5. Effect of hatch spacing on RD for three parts printed using the same laser power and scanning speed (150 W and 300 mm/s, respectively). A smaller hatch spacing led to lower densification due to more intensified keyhole porosity formation.

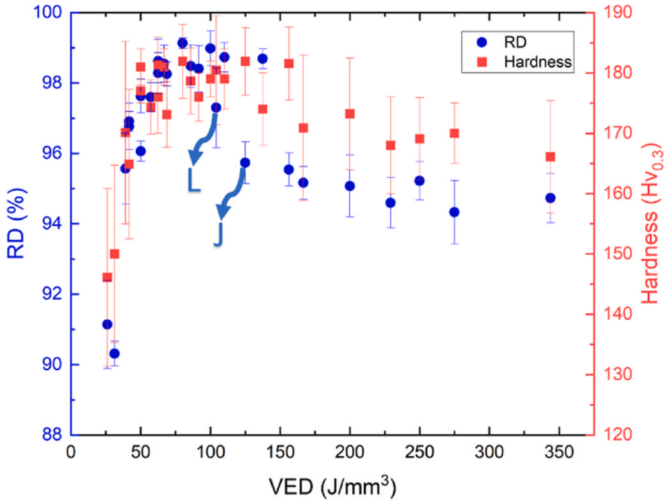

Fig. 6. The variation in relative density (RD) and microhardness of samples based on the VED.

at other scanning speeds. The variations in the microhardness values could be related to two factors that play significant roles. Densification level is a deciding factor in low VED. As the VED increases, the hardness elevates with a trend like the one observed on RD. That is, higher RD leads to higher hardness values. On the other hand, at low VED, where densifications deteriorate mainly due to lack of fusion and irregular porosities, there is less material to counteract the indentation during the test, which causes lower hardness values. In addition, the high probability of the presence of pores and elongated holes below the surface reduces the stiffness of the workpiece locally, as the test specimen can penetrate deeper into the material and show larger levels of uncertainty.

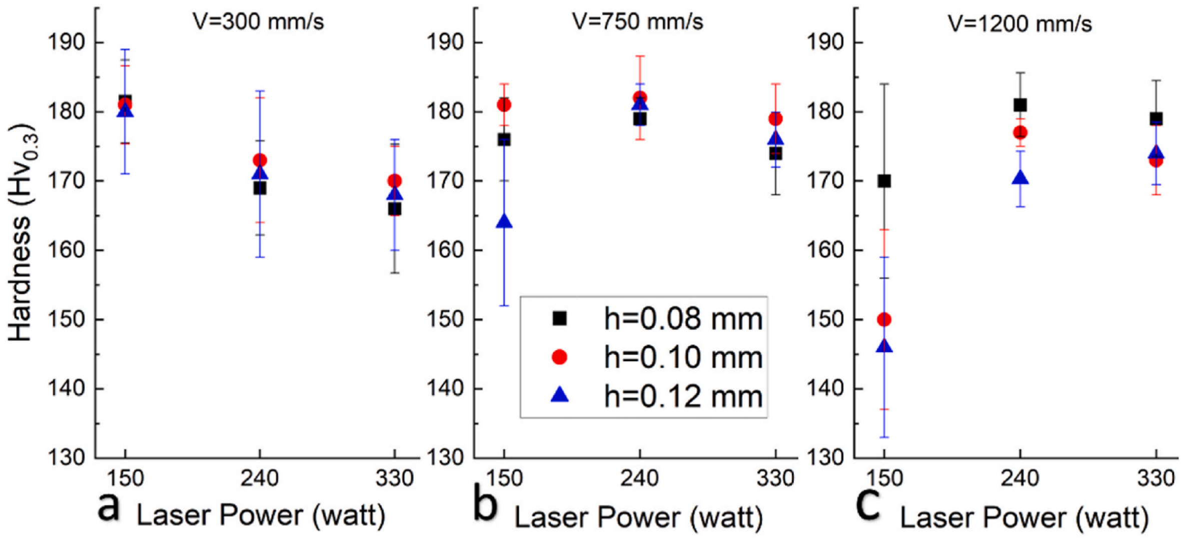

Fig. 7. Microhardness of samples based on laser power and hatch spacing at three exploited scanning speeds.

3.1.3. *Surface roughness*

The arithmetic mean height (Ra) was measured on the top and side surfaces of the samples, and the averaged measurements are depicted in Fig. 8 versus VED and in Fig. 9 based on the employed process variables. Considering the surface roughness of side walls, it is observed that the function of side surface roughness versus the VED has an increasing trend. However, although the arithmetic mean height on top surface for coupons fabricated by very high VEDs are significantly lower than others, there is a fluctuation in top surface roughness for other samples as the VED increases. Hence, it seems more logical to evaluate the roughness on top surfaces based on the effect of each single process variable. At low and medium scanning speeds, the increase in the laser power led to a significant decrease in Ra at all hatch spacings. The improved surface quality at high laser powers (at constant scanning speed and hatch spacing) is attributed to the expanded melt pool [48], providing a better overlap between adjacent scan tracks. Furthermore, as discussed in Ref. [49], higher laser powers generate a longer solidification time due to increased initial temperature, enabling the melt pool to spread and cover neighboring powders and previously solidified tracks (as also shown in Fig. 10). Additionally, the increased temperature reduces the surface tension of the liquid Fe–Ni alloy, enhancing the spreadability of the molten material. Concerning the roughness of the side surface, it is challenging to attribute a significant effect to individual process parameters. The results presented in Fig. 9 indicate that high laser powers increased the roughness of the side surface at low scanning speeds. This observation can be explained by the expansion of the melt pool, leading to increased lateral heat conduction. Consequently, powder particles tend to sinter to the side walls (Fig. 11). Likewise, the increasing trend of side surface roughness, as can be observed in Fig. 8, may be elucidated by heightened heat input to the material at elevated VEDs, thereby fostering more extensive lateral heat conduction.

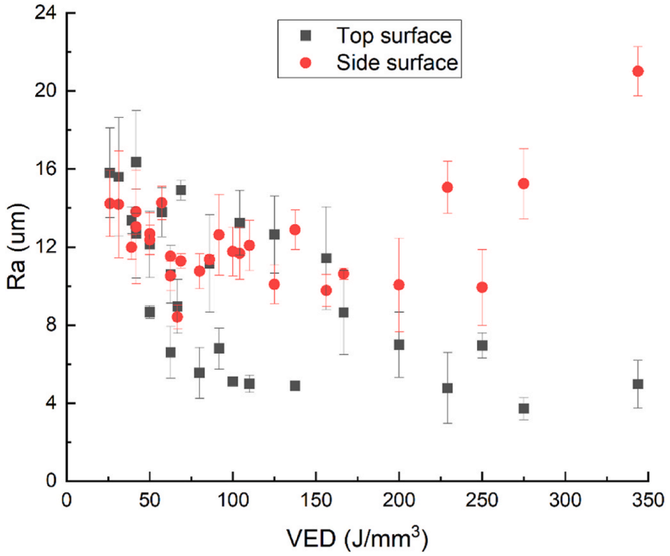

Fig. 8. Arithmetic mean height (Ra) of top and side surface of samples versus VED.

To assess the overall surface roughness achieved in the samples, roughness grade numbers [40] were utilized. Based on this classification, Ra values ranging from 3.2 to 6.3 μm were categorized as N8, while values between 6.3-12.5 μm and 12.5–25 μm were classified as N9 and N10, respectively. Table 2 demonstrates that the side wall surface roughness in all samples is generally high. Only a few samples achieved low surface roughness (grade N8) on the top surface. These samples were associated with hatch spacings of 0.08 and 0.1 mm. From the surface quality perspective, samples A, B, C, P, Q, S, and T (as also specified in Table 2) possessed the lowest surface roughness. By simultaneous consideration of the densification level and surface quality, the optimum samples were narrowed down to samples P, Q, S, and T. In the following, only these samples are subjected to magnetic properties investigations.

3.2. *D.C. Magnetic properties*

The magnetic properties of the optimal samples were examined in both as-built and heat-treated conditions to investigate the impact of process parameters and post-processing heat treatment on magnetic saturation, permeability, and coercivity in the D.C. mode. Magnetic properties can be classified into two categories: intrinsic properties, which are independent of the metallurgical condition of the material, and extrinsic properties, which are sensitive to the metallurgical condition. Extrinsic properties encompass factors such as grain size, grain shape, grain orientation, concentration and distribution of lattice imperfections, residual stresses, and atomic ordering. Understanding these extrinsic properties is crucial as they significantly influence the overall magnetic behavior of the material [14].

The Curie temperature and saturation magnetization are two magnetic properties that are not influenced by the structure of the materials.

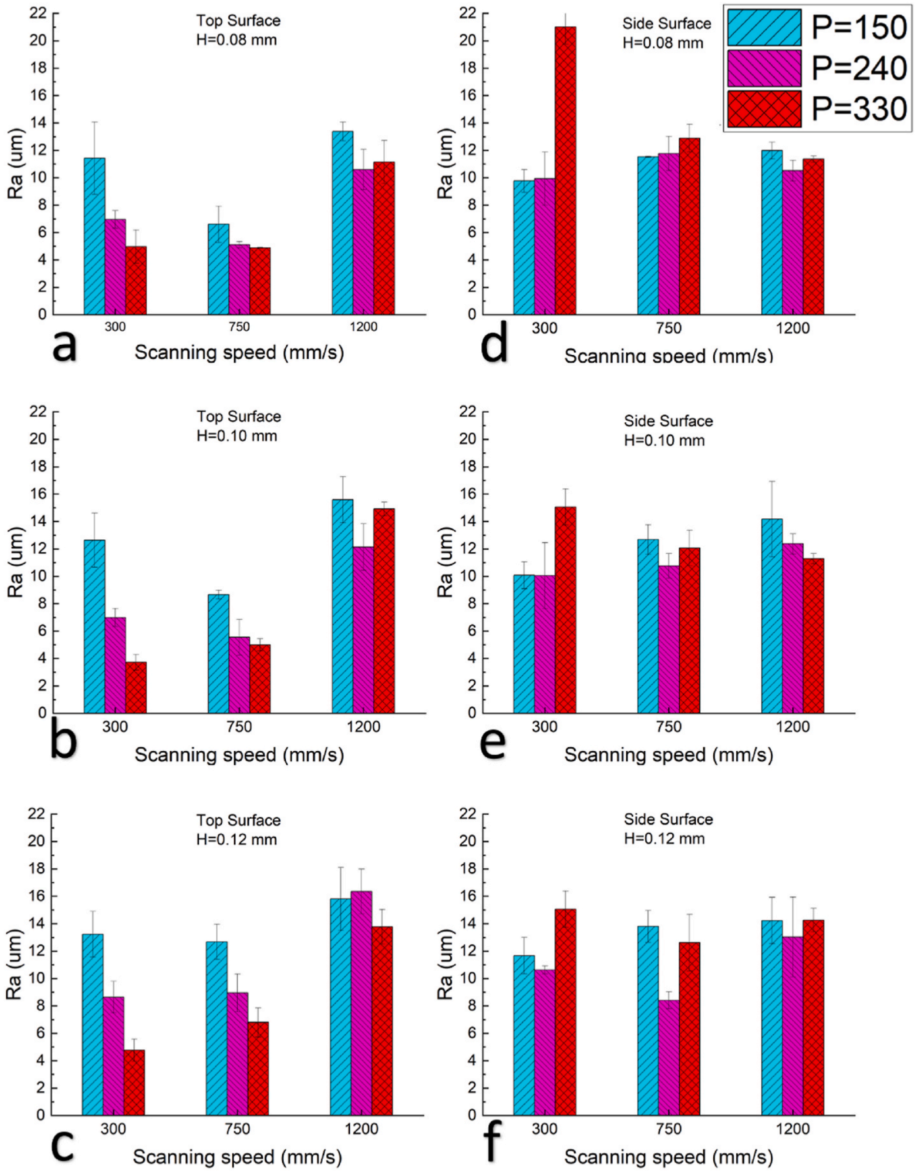

Fig. 9. Average arithmetic mean height (Ra) on the top surface (a-b-c) and the side surface (d-e-f) of coupons with different scanning speeds and laser powers at hatch spacings of (a, d) 0.08, (b, e) 0.10, and (c, f) 0.12 mm.

In this study, only the saturation magnetization was measured. The initial magnetization curve of the samples in both as-built and heat-treated conditions is presented in Fig. 12. The relative permeability (μ_r) is calculated and shown in Fig. 13 using the following equation:

$$\mu_r = 1 + B/\mu_0 H \tag{3}$$

where $\mu_0 = 4\pi \times 10^{-7}$ N/A^2 represents the permeability of free space, and B denotes the magnetic induction corresponding to the applied magnetic field (H). The maximum measured value of relative permeability represents the maximum permeability (μ_{max}), while the permeability at H = 40 A/m is referred to as the initial permeability (μ_{40}).

The saturation magnetization of the commercial alloy produced by conventional methods is just above 1.6 T [41]. Referring to Fig. 12, the highest field strength for as-built samples at the inducting field of 10000 A/m is achieved in sample #T, equal to 1.58 T, which is consistent with the high purity of the feedstock and low amount of porosity in this sample (Table 3). In another study on LPBF processing of the same alloy, a saturation magnetization equal to 1.5 T was reported [50]. Although saturation induction is considered an intrinsic property of the Fe–50Ni alloy, the magnetic behavior prior to saturation is structure-sensitive. Becker and Döring [51] showed that the route toward saturation is affected by the level of porosity, non-magnetic inclusions, and the stress field around dislocations and proposed a model for defining magnetization against the induction field as follows:

$$M(T) = M_s(T)\left[1 - \frac{\alpha}{H} - \frac{\beta}{H^2} - \dots\right] + X_0 H \tag{4}$$

where α, β, and X_0 are constants. β is linked to the stress field around dislocations, while α is related to the porosity of samples and nonmagnetic inclusions as well as the stress field around dislocations [14].

In applications demanding soft magnetic materials, besides having a high saturation magnetization, it is desirable to have higher maximum permeability (μ_{max}) and lower coercivity. Based on the information provided in Table 4, it can be observed that there are multiple samples exhibiting magnetic properties that are nearly identical in terms of μ_{max} and coercivity in the as-build condition. The variations in μ_{max} and coercivity between different samples are less than 8% and 7%, respectively. It is worth noting that these values are significantly inferior to

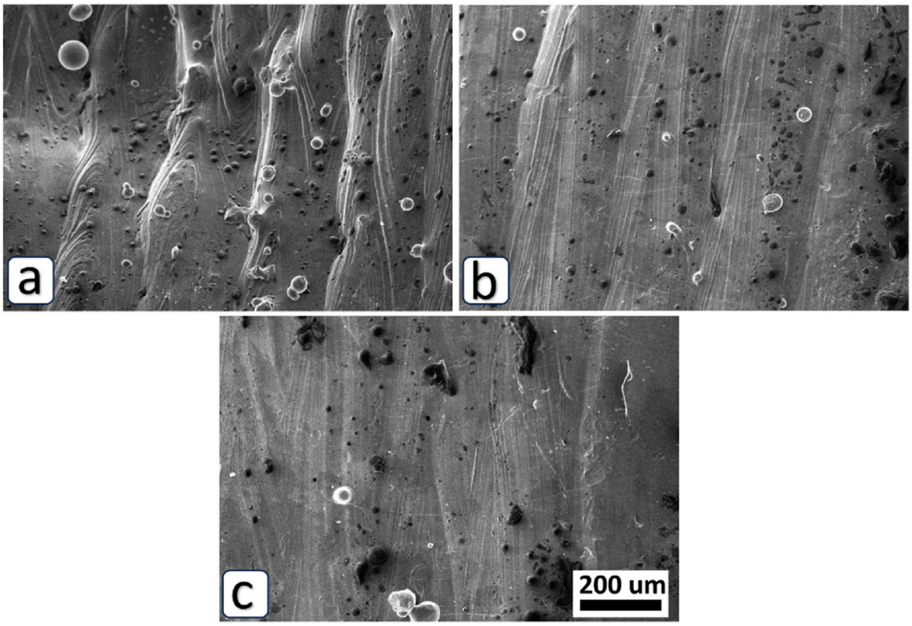

Fig. 10. SEM micrographs from the top surface of samples manufactured using a laser power of: (a) 150, (b) 240, and (c) 330 W. The scanning speed and hatch spacing were 300 mm/s and 0.12 mm for all three samples. Increasing the laser power almost vanishes the peaks and valleys observed at P = 150 W and improves the surface smoothness due to lower surface tension at elevated temperatures and better spread of melt pool.

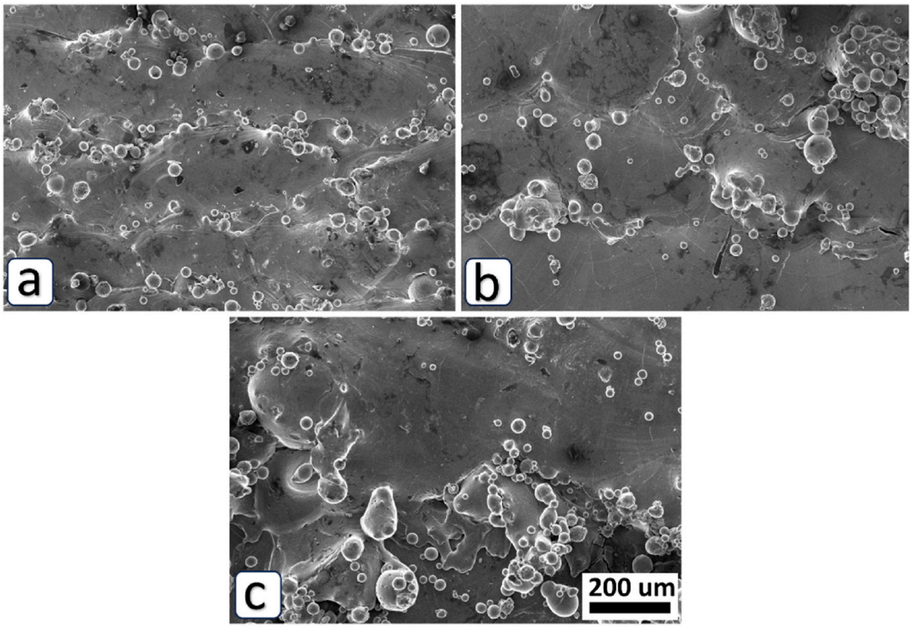

Fig. 11. SEM micrographs from the side surface of samples manufactured using a laser power of: (a) 150, (b) 240, and (c) 330 W. The scanning speed and hatch spacing were 300 mm/s and 0.08 mm for all three samples, respectively.

those reported for the same alloy in the wrought condition, which typically ranges from 2500 to 3000 for initial permeability and around 17000 for maximum permeability [14]. However, the achieved maximum permeability (μ_{max}) in the as-built samples aligns well with the findings of Mazeeva et al. [31], reporting a maximum permeability close to 1000 times that of free space.

Recalling the Becker and Döring theory in other words, it is proved that the magnetic behavior is primarily influenced by the grain size, porosity, and dislocation density [14,52]. Fig. 14 presents the inverse pole figure (IPF-X and IPF-Z) maps of different samples in the as-built condition. In Table 5, it is evident that the average grain size in all samples remains similar regardless of the employed process parameters. Additionally, the calculated average density of dislocations for all samples shows consistency, with negligible differences. Hence, these microstructural observations support the similarity in magnetic properties of samples in the as-built condition. However, slight deviations in the magnetic properties could be attributed to variations in microstructural texture across different samples. The XRD results of as-built samples, depicted in Fig. 16, provide insights into the texture as well as IPF texture plots. The {111} to {100} peak ratio serves as an indicator of the texture, where {111} and {100} represent the planes normal to the directions with the easiest and hardest magnetization in FCC

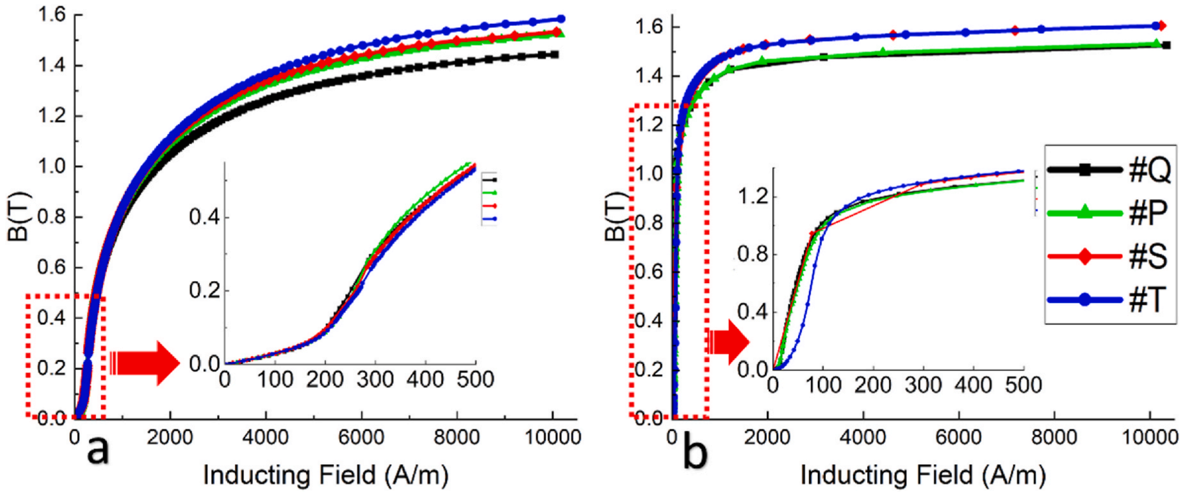

Fig. 12. Initial magnetization curve of (a) as-built and (b) heat-treated toroids in the D.C. mode.

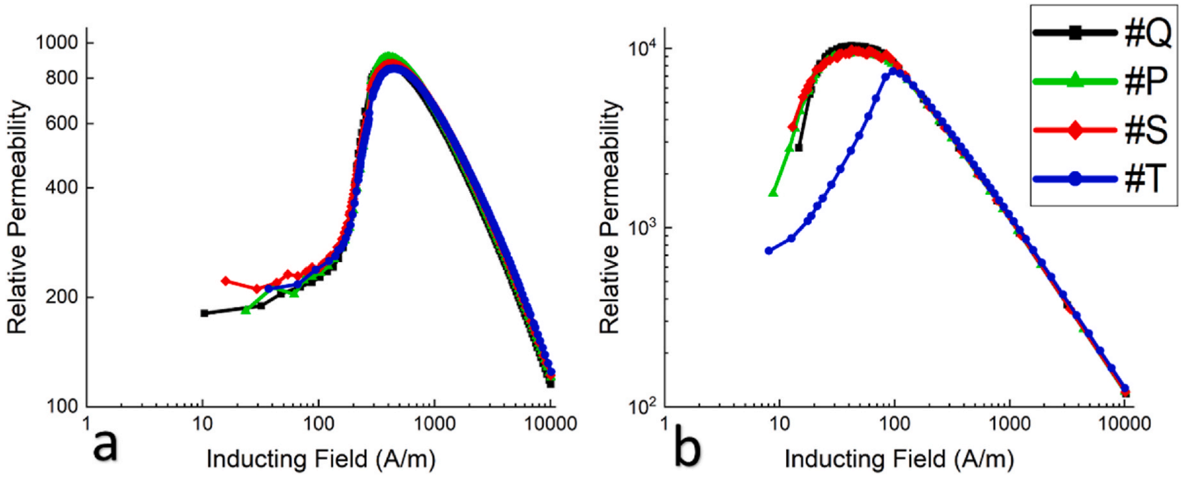

Fig. 13. Relative permeability of samples in the (a) as-built and (b) heat-treated conditions.

Table 4
Process parameters and magnetic properties of samples.

Sample	Process parameters			RD%	μ_{40}	μ_{max}		Coercivity (A/m)	
	P(watt)	V(mm/s)	h(mm)		AB	AB	HT	AB	HT
#Q	240	750	0.1	99.2	175	878	10371	262.3	44.4
#P	240	750	0.08	99.3	154	916	9448	272.3	47.8
#S	330	750	0.08	99.1	203.0	876	9368	277.9	75.2
#T	330	750	0.1	98.9	202.1	852	7459	284.2	84.1

structures, respectively. The significant differences in this ratio among different samples are evident in Fig. 16, accounting for the distinguished differences in the magnetic properties of samples in the as-built state. The increase in the VED by either raising the laser power from 240 W to 330 W or reducing hatch spacing leads to a decrease in the {111} to {100} peak ratio and weakens the easy-axis magnetization orientation on the vertical section of cubes, corresponding to the magnetization section of the toroids. Conversely, altering the hatch spacing does not have a substantial impact on the texture compared to changes in the laser power. By considering all magnetic properties, sample Q can be referred to as the optimum sample with the best possible combination of low coercivity and high μ_{max} in the as-built condition.

As a side note, the XRD patterns provide evidence that the resulting microstructure exclusively consists of the FCC phase. This observation corroborates previous research findings regarding the Fe–50Ni alloy produced through LPBF [31] or DED [53] techniques. It is well-known that the equilibrium crystal structure of Fe–50Ni is an ordered tetragonal L1$_0$ phase referred to as Elinvar [54]. However, due to the significantly limited atomic mobility of Fe and Ni atoms at low temperatures, with an estimated atomic jump frequency of one jump per 10^4 years at 300 °C [55], it is expected that a disordered cubic crystal structure, known as A1, forms (see Fig. 17).

3.3. A.C. Magnetic performance

The A.C. magnetic performance of samples was assessed across a wide frequency range. The total loss per unit mass of as-built samples when delivering a flux density equal to 0.5 and 1 T are measured and

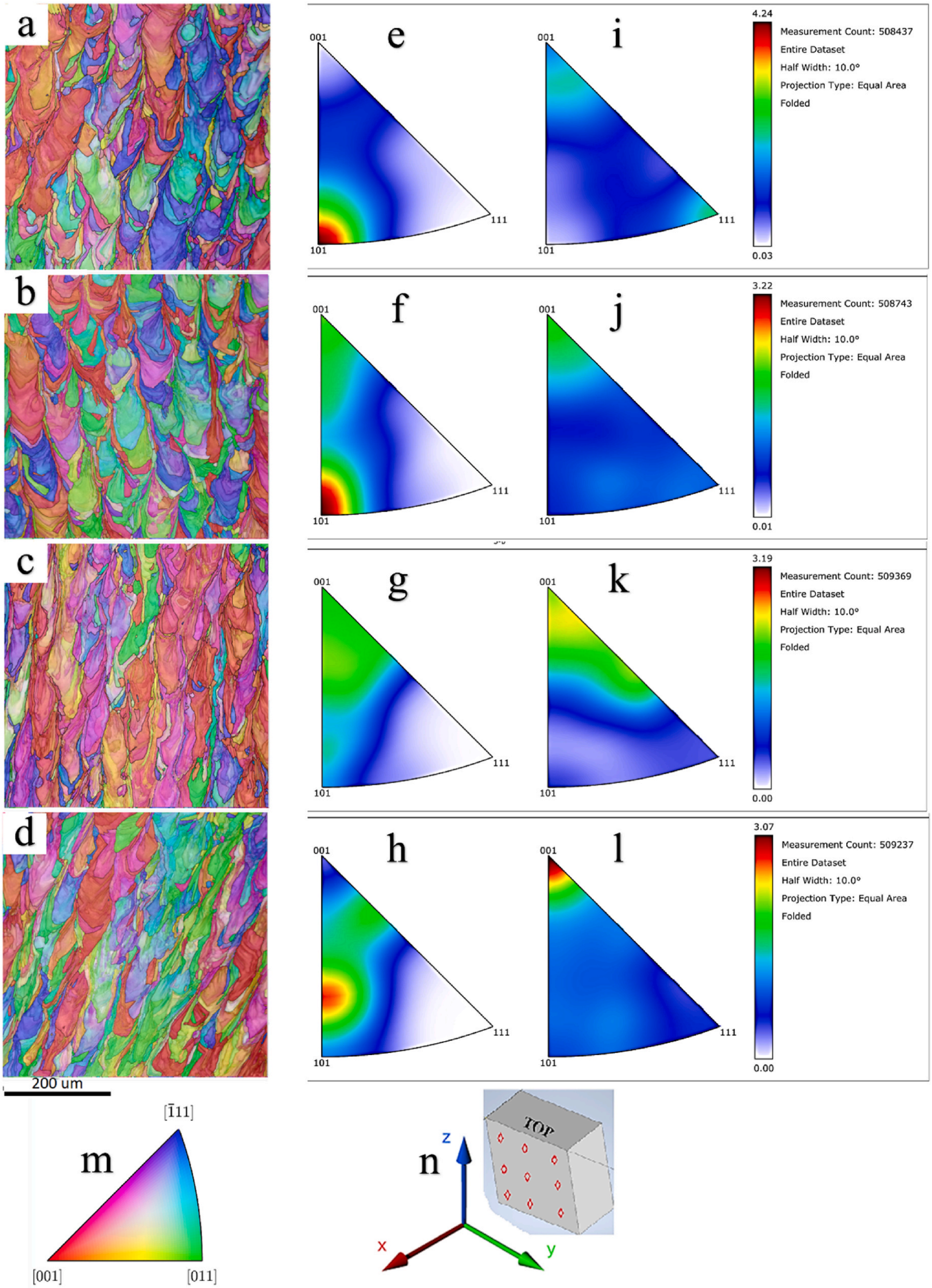

Fig. 14. EBSD results for as-built samples. (a–d) IPF-X maps of the YZ section of samples Q, T, P, and S. (e–h) Texture plot of YZ sections toward Z-direction (building direction). (i–l) Texture plot of YZ sections toward the X-direction (Corresponding to magnetization direction in toroids; see Fig. 1). (m) Color scheme for Inverse pole figures, and (n) measured section coordinate axes.

Table 5

Statistics of GND densities (m^{-2}) as well as the average grain size of samples in the as-built and heat-treated conditions.

Name	As-built				Heat-treated			
	Average (× 10^{13})	Median (× 10^{13})	Maximum (× 10^{13})	Average Grain Size (um)	Average (× 10^{13})	Median (× 10^{13})	Maximum (× 10^{13})	Average Grain Size (um)
Q	6.1	4.56	60	24.4	4.4	3.35	40	25.0
T	6	4.46	59	25.2	4.2	3.24	42	27.4
P	6.1	4.48	63	24.2	3.5	2.59	40	28.2
S	6.2	4.60	60	29.0	5.5	4.05	46	26.2

depicted in Fig. 18.

In alternating current (AC) applications, ferromagnetic materials experience the generation of an electromagnetic force (emf), inducing eddy currents in conductive materials. These eddy currents, along with hysteresis effects, contribute to energy losses in the material. In the case of a sinusoidal inducting field, the calculation of classical eddy-current loss is determined as [56]:

$$W_{ec} = \frac{\pi^2 B^2 t^2 f^2}{\beta \rho} \tag{6}$$

where $\boldsymbol{B}$ is the maximum inducting field (T), $\boldsymbol{t}$ is the cross-section dimension (m), $\boldsymbol{f}$ is the frequency, $\boldsymbol{\rho}$ is the electrical resistivity (Ω.m), and $\boldsymbol{\beta}$ is the geometry factor. However, by subtracting the hysteresis loss (W_h) from the total loss (W_{total}), it is revealed that in spite of the formula of Eq. (6), the eddy-current loss is not proportional to B^2. To address this commonly observed discrepancy, the total loss is defined as follows:

$$W_{total} = W_h + W_{ec} + W_a \tag{7}$$

in which $\boldsymbol{W_a}$ is called anomalous loss (excess loss). Eq. (6) holds true under the condition that B is linearly proportional to H and assumes a uniform penetration of the magnetic field throughout the entire cross-section of the material. However, in reality, the penetration of the magnetic field is restricted due to the shielding effects of eddy currents, and the eddy currents are localized around magnetic domain walls. Therefore, Eq. (6) does not account for these localized effects and the non-uniform distribution of eddy currents. The traditional viewpoint, based on Eq. (6), suggests that in the absence of excess loss, the total loss per cycle Should exhibit a linear relationship with frequency.

When comparing the as-built samples, notable performance differences are evident. Among them, sample Q, which demonstrated the best performance in the DC mode, exhibited significantly higher losses than the other samples at 0.5 T and 1T. This discrepancy can be explained by the presence of a larger proportion of <111> crystallographic orientation on the XY section of the toroid that is perpendicular to the magnetization direction (Z direction), compared to the other three samples (see Fig. 16). In the D.C. mode, the preferred texture facilitates easier magnetization and demagnetization (lower coercivity) for sample Q. However, under an A.C. field, the presence of <111> crystallographic orientation allows for greater mobility of domain walls, resulting in higher losses. On the other hand, samples with a higher orientation along the hard magnetization axis (indicated by the <200> crystallographic direction in Fig. 16) tend to rely on the less energy-intensive spin rotation mechanism, replacing the domain wall motion mechanism, especially at higher frequencies [57]. This can explain the differences in losses perceived among the samples at 1 T, where the movement of domain walls is preceded by the rotation of spins within the domains, particularly at higher frequencies where spin rotation becomes the predominant mechanism of magnetization. In addition, while the dynamic magnetic behavior of samples approximately follows a linear relationship with frequency at flux density of 0.5 T, the trend obviously deviates from linearity at higher flux density. The classical eddy-current loss presented in Eq. (6) is defined and calculated based on the domain-wall motion mechanism in ferromagnetic materials. At low external magnetic fields, the domain wall motion mechanism dominates, therefore it is expected that the loss obeys Eq. (6) and total loss per cycle exposes a linear relationship with working frequency. However, when the external magnetic field approaches the saturation point, the less energy intensive spin rotation mechanism substitutes [57], and therefore the classical eddy current loss equation is not valid anymore.

3.4. Effect of heat treatment

One coupon and one toroid for each set of process variables were heat treated according to the cycle shown in Fig. 1(d). In the following, the effect of heat treatment on mechanical and magnetic properties is discussed.

3.4.1. Effect of HT on hardness

Fig. 19 compares the hardness of samples in the as-built and heat-treated states. The hardness of heat-treated samples is 18–22% lower than the corresponding as-built ones. The decline in hardness is believed to be attributed to the reduction of the density of GNDs in the microstructure (see Table 5) and the slight grain growth based on the Hall-Petch strengthening mechanism [58] as follows:

$$HV = H_0 + k_H d^{\frac{-1}{2}} \tag{5}$$

where $\boldsymbol{H_0}$ and $\boldsymbol{k_H}$ are constants, and $\boldsymbol{d}$ represents the average grain size. Despite a significant decrease in hardness as opposed to the as-built condition, all heat-treated samples still exhibit superior hardness compared to the wrought alloy. (ASTM-A753, type 2, after 2–4 h of heat treatment at 1175 °C), which is ~90 HV [47]. Also, Table 6 provides the tensile test results for sample Q alongside the minimum requirements specified by the ASTM standard. This comparison indicates that the optimal sample regarding the magnetic characteristics not only exhibit acceptable magnetic performance but also delivers the necessary mechanical properties.

3.4.2. Effect of HT on D.C. Magnetic properties

Figs. 12(b) and 13(b) illustrate the initial magnetization and relative permeability of samples after heat treatment. In addition, the magnetic properties of the samples have been summarized in Table 4. As stated before, saturation magnetization is the intrinsic property of each ferromagnetic material and for Fe–50Ni alloy it is just above 1.6 T [41]. Similar to the as-built condition, the highest magnetization is recorded for sample T (1.6 T), consistent with the purity of the feedstock and low amount of porosity. On the other hand, the route toward the saturation point is a structure-sensitive property and is a function of microstructural impurity and stress field around dislocations [51]. There is a significant decrease in coercivity and a substantial increase in permeability across all examined samples. The heat-treated samples exhibit maximum permeability values in the range of 7500–10370, demonstrating an increase of at least 50% compared to the maximum permeability reported by Mazeeva et al. [31], who conducted vacuum heat treatment on their samples. This significant difference can be attributed to various factors, including the heating and cooling rates employed during the heat-treatment process and the chemical composition of the initial powder used. Additionally, the use of an Argon and Hydrogen

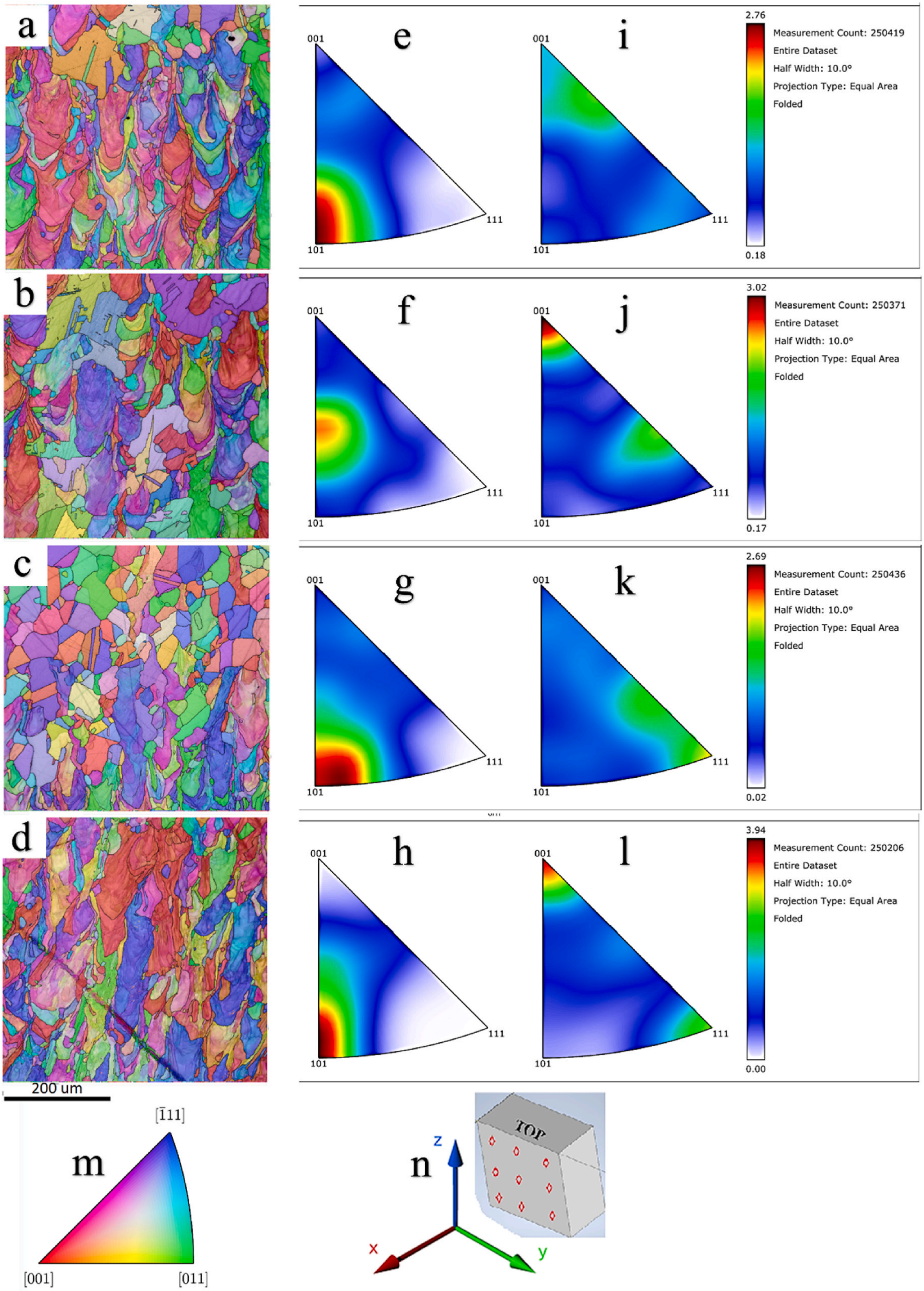

Fig. 15. EBSD results for heat-treated samples. (a–d) IPF-X maps of the YZ section of samples Q, T, P, and S. (e–h) Texture plot of YZ sections toward Z-direction (building direction). (i–l) Texture plot of YZ sections toward the X-direction (Corresponding to magnetization direction in toroids; see Fig. 1). (m) Color scheme for Inverse pole figures, and (n) measured section coordinate axes.

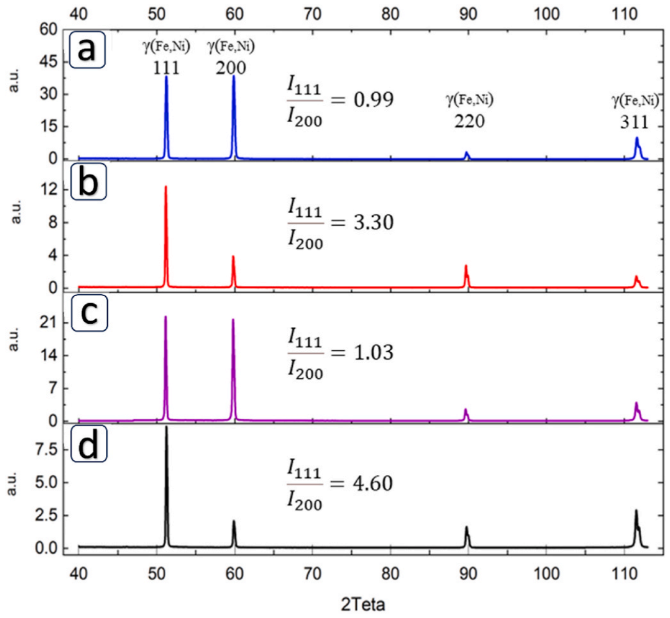

Fig. 16. XRD patterns of sample: (a) S, (b) P, (c) T, and (d) Q in the as-built condition. All samples possess an FCC-disordered phase of Fe and Ni atoms. The ratio of crystals oriented toward the easy axis of magnetization (<111>) to the crystals oriented toward the hard axis of magnetization (<200>) is calculated and depicted for each sample.

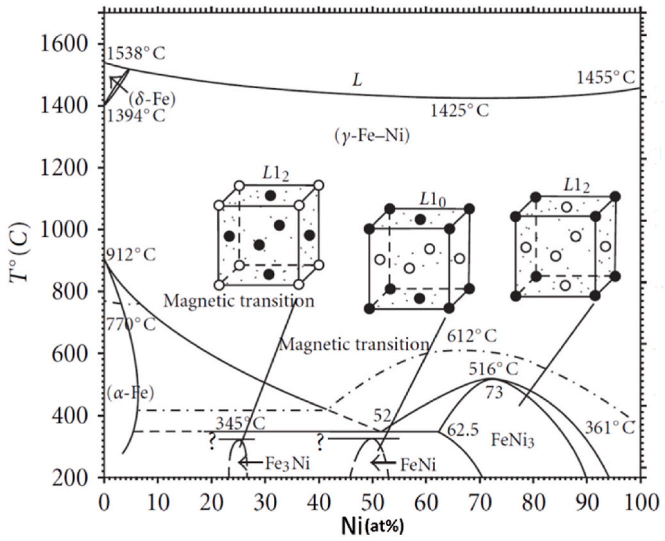

Fig. 17. Phase diagram of Fe–Ni binary alloys adapted from Ref. [54]. Hollow spheres represent Ni atoms, while solid ones represent Fe atoms.

mixture as the shielding atmosphere during heat treatment in this study could contribute to the higher permeability observed. The reducing gas (H_2) reacts with insoluble carbon, oxygen, and nitrogen impurities existing in the material, thereby reducing their concentrations as potential pinning sites for Bloch walls [41]. Considering the consistency of relative density before and after HT and not detecting a notable increase in grain size after HT (see Table 6), the significant reduction of dislocation density after heat treatment justifies the evident jump in permeability and substantial drop in coercivity, where the lowest value is measured for sample Q (44 A/m).

Fig. 15 showcases the IPF-X and IPF-Z maps of the optimized samples following heat treatment. Despite subjecting the samples to elevated temperatures for a considerable time during the heat treatment process, exceptional resistance to grain growth was detected. However, a comparison of grain morphology before and after heat treatment reveals a transformation from elongated grains to more equiaxed grains, indicating the occurrence of recrystallization and subsequent grain growth during the thermal cycle. Also, comparing texture plots of as-built and heat-treated samples reveals that the crystallography orientation on the YZ section has subtly changed as some grains have rotated from a mixture of [001] and [111] directionality to a mixture of [001] and [112] directions (in samples Q and T) or a mixture of [112] to [111] in sample P and a strong peak of [001] with a significant peak of [111] directionality in sample S. The average grain size in the respective samples has only increased by 2–16%, although a reduction of 10% is observed in sample S which is believed to be due to recrystallization. Consequently, as noted previously, the changes in grain size alone cannot account for the significant enhancement in permeability and the noticeable reduction in coercivity. To shed light on this, Fig. 20 presents the distribution of dislocations in the heat-treated samples, while the average dislocation density is provided in Table 5. Evidently, the heat treatment process has led to a substantial decrease in dislocation density, which serves as the underlying cause for the discovered improvement in the magnetic behavior of the material, recalling the Kersten's theory which states dislocations, grain boundaries, porosities, and inclusions can act as potential pinning sites for domain walls [61]. Since the size of porosities is not comparable to the width of the domain wall in this alloy (tens of microns compared to a domain wall width of approximately 0.21 μm [50]), they do not appear to have an influence

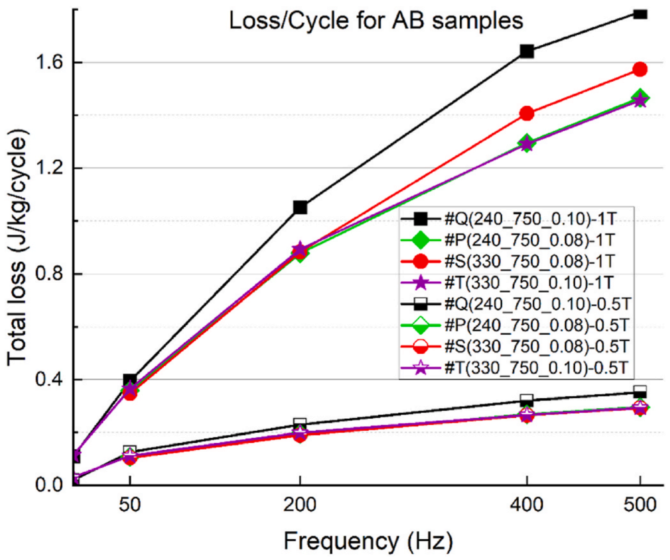

Fig. 18. Total loss per cycle of as-built samples when delivering 0.5T and 1T.

Table 6
Results of the tensile test for sample Q in comparison with the same material as per ASTM A753 standard.

Sample	Process Variables			VED (J/mm^3)	Yield Strength (MPa)	Ultimate Tensile Strength (MPa)	Elongation at break (%)
	P (W)	V (mm/s)	H (mm)				
#Q	240	750	0.10	80	374.9 ± 4.0	484.9 ± 5.0	29.3 ± 1.3
–	Fe–49Ni (ASTM A753) in annealed condition [47]				165	441	35

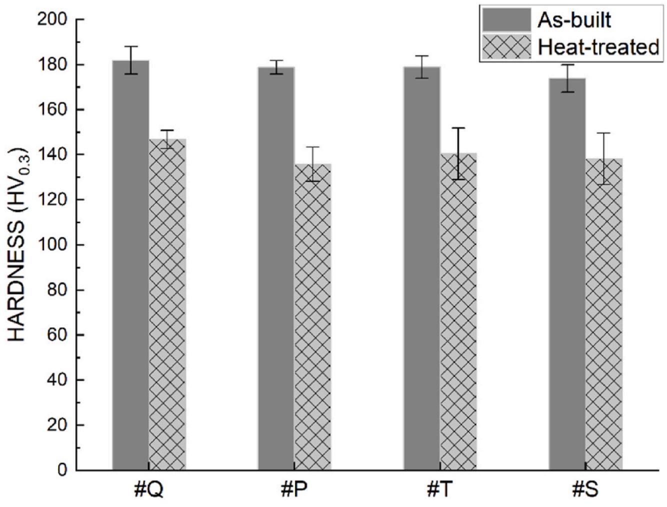

Fig. 19. Microhardness of selected samples before and after heat treatment.

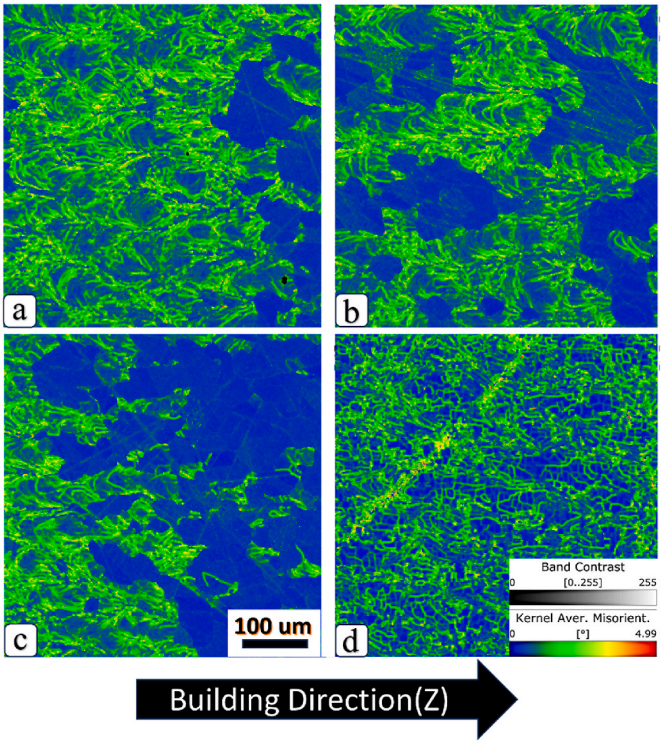

Fig. 20. Kernel average misorientation (KAM) maps of samples: (a) Q, (b) T, (c) P, and (d) S in the heat-treated condition.

on the magnetization of this alloy, both in the as-built and heat-treated conditions.

Upon comparing the magnetic properties of the heat-treated samples, as presented in Table 4 and Fig. 13, it can be inferred that sample Q demonstrated superior performance not only among the optimal samples in the as-built condition but also in the heat-treated state. Its coercivity decreased from 262 A/m to 44 A/m after heat treatment, though this value is approximately twice the intrinsic coercivity of the wrought alloy [41]. In terms of maximum permeability (μ_{max}) and coercivity, sample Q outperforms the other heat-treated samples by 9–28% and 8–90%, respectively. Conversely, sample T exhibits the worst magnetic properties both in the as-built and heat-treated conditions. The laser power of 240 W, scanning speed of 750 mm/s, and hatch spacing of 0.1 mm employed for printing sample Q resulted in high densification levels and low surface roughness and also yielded the most favorable semi-static magnetic properties in as-built and heat-treated conditions.

3.4.3. *Effect of HT on A.C. Magnetic properties*

The total loss per unit mass of the as-built and heat-treated samples while delivering flux densities equal to 0.5 T and 1 T were measured and the energy loss per unit mass in each cycle is depicted in Fig. 21. Due to the lack of published studies investigating the dynamic performance of this alloy processed by LPBF or DED across various frequencies, the total loss of the samples at 50 Hz was compared to Fe–Si alloys fabricated through the L-PBF process as reported in the literature [13,59,60], as well as a laminated core made of wrought Fe–50Ni alloy [56] (see Table 7).

It becomes apparent that the energy loss in the heat-treated samples is notably lower than that of the as-built ones at low flux densities. However, as the flux density increases to 1 T, this difference becomes less pronounced, and particularly at higher frequencies, no significant disparity in total loss is observed between the heat-treated and as-built ones. These findings are consistent with the results of [62], reporting nearly identical dynamic losses of pure iron before and after stress relief treatment at a flux density of 1.5 T.

According to the classical eddy-current loss (Eq. (6)), it is expected that the total loss per cycle exhibits a linear relationship with frequency. Such behavior can be discerned in the total loss of heat-treated samples at $B = 0.5$ T and with some approximation at $B = 1$ T. Since the loss does not obey Eq. (6) perfectly, based on Eq. (7), it can be split into hysteresis loss per cycle (constant regardless of frequency), classical eddy-current loss per cycle (linearly proportional to frequency), and excess loss (proportional to $f^{\,n}$, where $n \sim 0.5$). Splitting the loss parameters in this way helps to conceive the concave shape of loss curves for as-built samples, as depicted in Fig. 21. The reason that as-built samples do not obey a linear increase in energy loss per cycle by raising the working frequency is that the width of magnetic domains within the microstructure is not constant, and as the frequency increases, more domains are activated, resulting in a reduction in the domain width [14,56,63]. Consequently, the reduced domain width leads to a lower average velocity of domain walls, yielding a less rapid increase in eddy current losses compared to what would be expected with a fixed number of magnetic domains, with regard to the fact that the total loss is proportional to the square of the domain wall velocity [63]. In other words, activating a greater number of magnetic domains in the microstructure leads to more deviation from the linear proportionality between total loss and frequency. Based on this theory, the more rapid growth of energy loss in heat-treated samples compared to their corresponding as-built ones is attributed to the existing less magnetic domain walls in the heat-treated state compared to the as-built scenario (due to a smaller stress state around dislocations and GND density) so that in elevated frequencies, when the flux density is equal to 1 T, no considerable decrease in energy loss is obtained by heat treatment. This fact criticizes the heat treatment since it declines the strength but does not yield significant improvements in the dynamic magnetic performance.

4. Conclusions

This study focused on the fabrication of Fe–50Ni alloy using laser powder bed fusion (LPBF) and analyzed its relative density, surface roughness, and magnetic properties. The results showed that high densification levels above 98.5% can be achieved by optimizing the process parameters. Surface roughness analysis indicated that increasing laser power at low and medium scanning speeds improved the top surface quality. While attributing specific effects to individual process parameters on side surface roughness was found to be challenging, the sidewall surface roughness was generally high.

The investigation of magnetic properties for the LPBF fabricated parts revealed a saturation point of 1.6 T, corresponding to the intrinsic

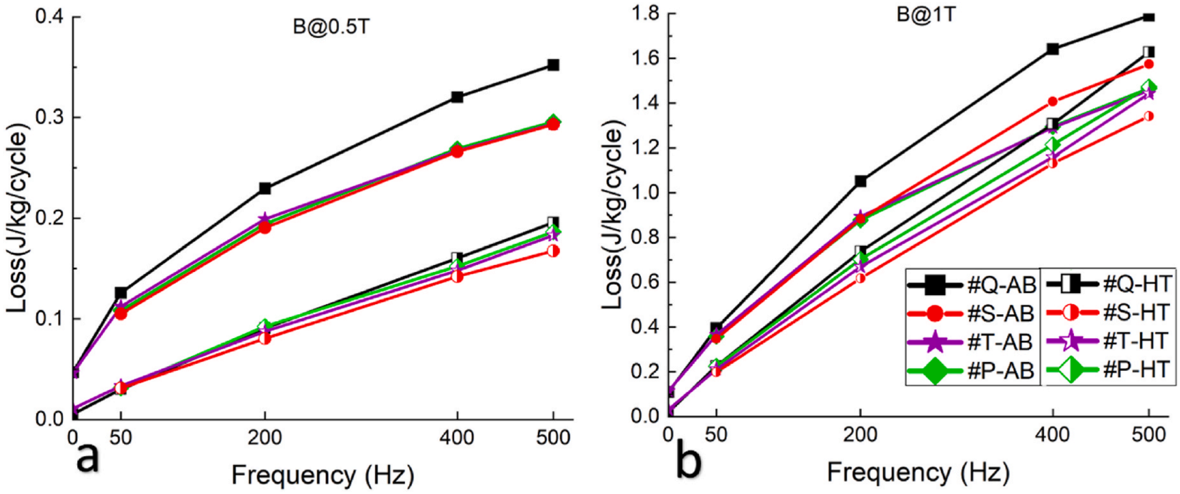

Fig. 21. Total loss per unit mass in 1 cycle for four samples in as-built and heat-treated conditions tested under a flux density of (a) 0.5 T and (b) 1 T. The intercept of curves by the vertical axis indicates the hysteresis loss value per cycle.

Table 7
Total loss at f = 50Hz and flux density = 1T in as-built and heat-treated states for the LPBF processed Fe–Si and Fe–Ni alloys as well as the commercial Fe–50Ni alloy.

Alloy	$B_{50\text{-}1}$(W/kg)	
	As-built	Heat-treated
Fe–50Ni (This study)	13.7–19.8	9.7–11.3
Fe–50Ni (commercial[a]) [56]	N/A	0.2
Fe-6.9Si [59,60]	4.3–6.1	2.2
Fe-3.7Si [13]	–	10.7–15.9

[a] Sheet thickness = 0.2–0.5 mm.

property of the alloy or falling within a 15% margin of this value at an induction field of 10^4 A/m. The as-built samples exhibited significantly lower initial and maximum magnetic permeability compared to the wrought alloy, while the heat-treated samples demonstrated a notable increase in permeability. The improved permeability of the heat treated samples is mainly attributed to the reduction of lattice strain and texture development during the heat treatment process as other factors like densification level and grain size did not alter notably. Sample Q showed the best combination of low coercivity and high maximum permeability among all as-built samples. This sample also featured the highest improvement in both parameters after heat treatment. Additionally, Sample Q satisfied the required mechanical properties in terms of strength and ductility and exhibited a hardness at least 50% higher than that of the commercial alloy.

Heat treatment had a prominent influence on the dynamic magnetic performance of samples. A substantial decrease in energy loss was observed after heat treatment, particularly at B = 0.5 T. However, as the frequency increased, the difference in energy loss between the heat-treated and as-built samples gradually diminished. While heat treatment played a role in reducing energy losses, its impact diminished at higher frequencies. This is because, in the as-built condition, a greater number of domain walls could be activated compared to the heat-treated state, leading to lower-than-expected losses in the as-built state. Sample Q, despite exhibiting the best D.C. magnetic properties, demonstrated the highest total loss among all samples. In contrast, Sample T, printed with higher laser power, displayed higher A.C. magnetic efficiency, particularly at elevated frequencies. The disparity in total loss can be attributed to the difference in crystallographic orientation among these samples, where Sample Q's texture favored energy-intensive domain wall motion, while Sample T's unmatched texture promoted lower energy expenditure through spin rotation. Findings of this study about the energy losses before and after heat-treatment encourage reconsideration of conducting heat treatment, specifically when the working frequency of the motor is beyond 400 Hz.

In conclusion, this study successfully fabricated Fe–50Ni alloy using LPBF, achieving satisfactory densification, surface roughness, and magnetic properties. These findings contribute to the understanding and advancement of additive manufacturing processes for magnetic materials.

CRediT authorship contribution statement

M. Ahmadnia: Conceptualization, Methodology, Writing – original draft, Formal analysis, Investigation. **E. Fereiduni:** Writing – original draft, Writing – review & editing, Investigation. **M. Yakout:** Writing – review & editing. **M. Elbestawi:** Writing – review & editing, Funding acquisition, Supervision. **R.K. R M:** Data curation. **G. Vakil:** Validation, Resources. **R. Muizelaar:** Supervision.

Declaration of competing interest

The authors declare that they have no known competing financial interests or personal relationships that could have appeared to influence the work reported in this paper.

Acknowledgment

The authors would like to express their gratitude to **Professor Hatem Zurob** from the Department of Materials Science and Engineering at McMaster University for his advice and for providing access to the heat-treatment facilities. They would also like to thank **Sofia Czerny-Holownia** for her assistance in implementing the heat treatment process. We highly value the assistance of **Dr. Liping Wang** from Stackpole International, for fruitful discussions concerning electric motors. Additionally, the authors acknowledge **Victoria M. Jarvis** from the MAX Diffraction Facility for providing XRD training, and **Dr. Ali Ghasemi** from AMG group at McMaster University for his guidance in sample preparation and material characterization.

This research was financially supported by the Natural Sciences and Engineering Research Council of Canada (NSERC) through its CREATE program led by York University.

References

[1] Henke M, et al. Challenges and Opportunities of very light high-performance electric Drives for aviation. Energies 2018;11. https://doi.org/10.3390/en11020344.

[2] Yang S, Tang Y, Zhao YF. A new part consolidation method to embrace the design freedom of additive manufacturing. J Manuf Process Oct. 2015;20:444–9. https://doi.org/10.1016/j.jmapro.2015.06.024.

[3] Atzeni E, Salmi A. Economics of additive manufacturing for end-useable metal parts. Int J Adv Manuf Technol Oct. 2012;62(9–12):1147–55. https://doi.org/10.1007/s00170-011-3878-1.

[4] Liu L, Ge T, Ngo KDT, Mei Y, Lu G-Q. Ferrite paste cured with ultraviolet light for additive manufacturing of magnetic components for power electronics; ferrite paste cured with ultraviolet light for additive manufacturing of magnetic components for power electronics. IEEE Magn Lett 2018;9:5102705. https://doi.org/10.1109/LMAG.2018.2822622.

[5] Ding C, Liu L, Mei Y, Ngo KDT, Lu G-Q. Magnetic paste as feedstock for additive manufacturing of power magnetics; Magnetic paste as feedstock for additive manufacturing of power magnetics. 2018. https://doi.org/10.1109/APEC.2018.8341075.

[6] Chicinas I, Pop V, Isnard O. Synthesis of the supermalloy powders by mechanical alloying. J Mater Sci 2004;39:5305–9.

[7] Chaudhary V, et al. Additive manufacturing of functionally graded Co–Fe and Ni–Fe magnetic materials. J Alloys Compd May 2020;823. https://doi.org/10.1016/j.jallcom.2020.153817.

[8] Kustas AB, et al. Characterization of the Fe-Co-1.5V soft ferromagnetic alloy processed by laser engineered net shaping (LENS). Addit Manuf 2018;21:41–52. https://doi.org/10.1016/j.addma.2018.02.006.

[9] Mikler CV, Chaudhary V, Soni V, Gwalani B, Ramanujan RV, Banerjee R. Tuning the phase stability and magnetic properties of laser additively processed Fe-30at% Ni soft magnetic alloys. Mater Lett Jul. 2017;199:88–92. https://doi.org/10.1016/j.matlet.2017.04.054.

[10] Mikler CV, et al. Laser additive processing of Ni-Fe-V and Ni-Fe-Mo Permalloys: microstructure and magnetic properties. Mater Lett Apr. 2017;192:9–11. https://doi.org/10.1016/j.matlet.2017.01.059.

[11] Dubinin ON, et al. Gradient soft magnetic materials produced by additive manufacturing from non-magnetic powders. J Mater Process Technol Feb. 2022;300. https://doi.org/10.1016/j.jmatprotec.2021.117393.

[12] Lamichhane TN, Sethuraman L, Dalagan A, Wang H, Keller J, Paranthaman MP. Additive manufacturing of soft magnets for electrical machines—a review. In: Materials today physics, vol. 15. Elsevier Ltd; Dec. 01, 2020. https://doi.org/10.1016/j.mtphys.2020.100255.

[13] Tiismus H, Kallaste A, Vaimann T, Rassõlkin A. State of the art of additively manufactured electromagnetic materials for topology optimized electrical machines. In: Additive manufacturing, vol. 55. Elsevier B.V.; Jul. 01, 2022. https://doi.org/10.1016/j.addma.2022.102778.

[14] Chen C. Magnetism and metallurgy of soft magnetic materials. North-Holland Pub. Co.; 1977.

[15] Buschow KHJ, De Boer FR. Physics of magnetism and magnetic materials. New York: Kluwer Academic/Plenum Publishers; 2003.

[16] Palousek D, Pantelejev L, Zikmund T, Koutny D. Processing of nearly pure iron using 400W selective laser melting – initial study. In: MM science journal, vol. 2017. FEBRUARY; Feb. 2017. p. 1738–43. https://doi.org/10.17973/MMSJ.2017_02_2016184.

[17] Letteneur M, Brailovsky V, Kreitcberg A, Paserin V, Bailon-Poujol I. Laser powder bed fusion of water-atomized iron-based powders. Journal of Manufacturing and Materials Processing Dec. 2017;1(23).

[18] Garibaldi M, Ashcroft I, Simonelli M, Hague R. Metallurgy of high-silicon steel parts produced using Selective Laser Melting. Acta Mater May 2016;110:207–16. https://doi.org/10.1016/j.actamat.2016.03.037.

[19] Goll D, et al. Additive manufacturing of soft magnetic materials and components. Addit Manuf May 2019;27:428–39. https://doi.org/10.1016/j.addma.2019.02.021.

[20] Yakout M, Elbestawi MA, Wang L, Muizelaar R. Selective laser melting of soft magnetic alloys for automotive applications. In: *Joint special interest Group meeting between euspen and ASPE*, nantes: joint special interest group meeting between euspen and ASPE; Sep. 2019 [Online]. Available: www.euspen.eu.

[21] P. Ohodnicki, "Soft magnetic alloys for electrical machine applications: basics, state of the art, and R&D opportunities".

[22] Krings A, Boglietti A, Cavagnino A, Sprague S. Soft magnetic material status and trends in electric machines. IEEE Trans Ind Electron Mar. 2017;64(3):2405–14. https://doi.org/10.1109/TIE.2016.2613844.

[23] Zhang B, Fenineche NE, Liao H, Coddet C. Magnetic properties of in-situ synthesized FeNi3 by selective laser melting Fe-80%Ni powders. J Magn Magn Mater Jun. 2013;336:49–54. https://doi.org/10.1016/j.jmmm.2013.02.014.

[24] Mikler CV, et al. Laser additive manufacturing of magnetic materials. JOM Mar. 2017;69(3):532–43. https://doi.org/10.1007/s11837-017-2257-2.

[25] Schönrath H, et al. Additive manufacturing of soft magnetic permalloy from Fe and Ni powders: control of magnetic anisotropy. In: Journal of magnetism and magnetic materials, vol. 478. Elsevier B.V.; May 15, 2019. p. 274–8. https://doi.org/10.1016/j.jmmm.2018.11.084.

[26] Zhang B, Fenineche NE, Liao H, Coddet C. Microstructure and magnetic properties of Fe-Ni alloy fabricated by selective laser melting Fe/Ni mixed powders. J Mater Sci Technol Aug. 2013;29(8):757–60. https://doi.org/10.1016/j.jmst.2013.05.001.

[27] Zhang B, Fenineche NE, Zhu L, Liao H, Coddet C. Studies of magnetic properties of permalloy (Fe30%Ni) prepared by SLM technology. J Magn Magn Mater Feb. 2012;324(4):495–500. https://doi.org/10.1016/j.jmmm.2011.08.030.

[28] Chaudhary V, Mantri SA, Ramanujan RV, Banerjee R. Additive manufacturing of magnetic materials. In: Progress in materials science, vol. 114. Elsevier Ltd; Oct. 01, 2020. https://doi.org/10.1016/j.pmatsci.2020.100688.

[29] Shishkovsky I, Saphronov V. Peculiarities of selective laser melting process for permalloy powder. Mater Lett May 2016;171:208–11. https://doi.org/10.1016/j.matlet.2016.02.099.

[30] Wang X, Wraith M, Burke S, Rathbun H, DeVlugt K. Densification of W-Ni-Fe powders using laser sintering. Int J Refract Metals Hard Mater Apr. 2016;56:145–50. https://doi.org/10.1016/j.ijrmhm.2016.01.006.

[31] Mazeeva AK, Staritsyn MV, Bobyr VV, Manninen SA, Kuznetsov PA, Klimov VN. Magnetic properties of Fe–Ni permalloy produced by selective laser melting. J Alloys Compd 2020;814(Jan). https://doi.org/10.1016/j.jallcom.2019.152315.

[32] Talaat A, et al. Review on soft magnetic metal and inorganic oxide nanocomposites for power applications. In: Journal of alloys and compounds, vol. 870. Elsevier Ltd; Jul. 25, 2021. https://doi.org/10.1016/j.jallcom.2021.159500.

[33] Metelkova J, Kinds Y, Kempen K, de Formanoir C, Witvrouw A, Van Hooreweder B. On the influence of laser defocusing in Selective Laser Melting of 316L. Addit Manuf Oct. 2018;23:161–9. https://doi.org/10.1016/j.addma.2018.08.006.

[34] Kluczyński J, Śniezek L, Grzelak K, Mierzyński J. The influence of exposure energy density on porosity and microhardness of the SLM additive manufactured elements. Materials Nov. 2018;11(11). https://doi.org/10.3390/ma11112304.

[35] Ferro P, Meneghello R, Savio G, Berto F. A modified volumetric energy density-based approach for porosity assessment in additive manufacturing process design Check for updates. The Internationa l Journal of Advanced Manufacturing Technology 2020;11(0):1911–21. https://doi.org/10.1007/sOOl.

[36] Carter LN, et al. Process optimisation of selective laser melting using energy density model for nickel based superalloys. Mater Sci Technol Jun. 2016;32(7):657–61. https://doi.org/10.1179/1743284715Y.0000000108.

[37] Adegoke O, et al. Influence of laser powder bed fusion process parameters on the microstructure of solution heat-treated nickel-based superalloy Alloy 247LC. Mater Charact 2022;183(Jan). https://doi.org/10.1016/j.matchar.2021.111612.

[38] IEC IEC. 60404-Part 4: methods of measurement of d.c. magnetic properties of magnetically soft materials." [Online]. Available: www.iec.ch/searchpub/cur_fut-f.htm; 2008.

[39] ASTM E8/E8M-21. Standard test methods for tension testing of metallic materials. ASTM International; 2021.

[40] Sharma PC. A textbook of production engineering. eleventh ed. New Delhi: S. CHAND & COMPANY LTD; 2009.

[41] Richard M. Bozorth, *ferromagnetism.* first ed. New Jersy: D. Van Nostrand Company, Inc.; 1956.

[42] ISO 4288:1996(E): geometrical Product Specifications (GPS)- Surface texture: profile method- Rules and procedures for the assessment of surface texture. International Standard Organization (ISO); 1996.

[43] He BB. Two-dimensional x-ray diffraction. second ed. John Wiley & Sons; 2018.

[44] IEC, "BS EN IEC 60404-Part 6: methods of measurement of the magnetic properties of magnetically soft metallic and powder materials at frequencies in the range 20 Hz to 100 kHz by the use of ring specimens. 2018.

[45] Yadroitsev I, Du Plessis A, Yadroitsava I. Basics of laser powder bed fusion. In: Fundamentals of laser powder bed fusion of metals. Elsevier; 2021. p. 15–38. https://doi.org/10.1016/B978-0-12-824090-8.00024-X.

[46] DebRoy T, et al. Additive manufacturing of metallic components – process, structure and properties. In: Progress in materials science, vol. 92. Elsevier Ltd; Mar. 01, 2018. p. 112–224. https://doi.org/10.1016/j.pmatsci.2017.10.001.

[47] ASM International. Special-purpose nickel alloys commercially pure nickel for electronic applications. 2000 [Online]. Available: www.asminternational.org.

[48] Yang T, et al. The influence of process parameters on vertical surface roughness of the AlSi10Mg parts fabricated by selective laser melting. J Mater Process Technol Apr. 2019;266:26–36. https://doi.org/10.1016/j.jmatprotec.2018.10.015.

[49] Balbaa M, Mekhiel S, Elbestawi M, McIsaac J. On selective laser melting of Inconel 718: densification, surface roughness, and residual stresses. Mater Des 2020;193(Aug). https://doi.org/10.1016/j.matdes.2020.108818.

[50] E. Urig. Additive Manufacturing of soft magnetic Fe50Ni. University of Virginia; 2020.

[51] Becker R, Doring W. Ferromagnetism. Berlin: Verlag. Julius Springer; 1939.

[52] Gasior W, Fima P, Moser Z. Modeling of the thermodynamic properties of liquid Fe-Ni and Fe-Co alloys from the surface tension data. Arch Metall Mater 2011;56(1):13–23. https://doi.org/10.2478/v10172-011-0002-3.

[53] Kim ES, Haftlang F, Ahn SY, Kwon H, Gu GH, Kim HS. Mechanical and magnetic properties of soft magnetic Fe–Ni permalloy produced by directed energy deposition processes. J Mater Sci Oct. 2022;57(38):17967–83. https://doi.org/10.1007/s10853-022-07110-1.

[54] Massalski TB, Murray JL, Bennett LH, Baker H. *Binary alloy phase diagrams*, illustrated, vol. 1. ASM; 1986.

[55] Scorzelli RB. A study of phase stability in invar Fe-Ni alloys obtained by non-conventional methods. 1997.

[56] Jiles D. Introduction to magnetism and magnetic materials. third ed. CRC Press; 2016.

[57] Chikazumi S. Physics of ferromagnetism. second ed. New York: Oxford University Press Inc; 1997.

[58] Furukawat M, Horita' Z, Nemoto M, Valiev RZ, Langdon TG. Microhardness Measurements and the Hall-Petch Relationship in an Al-Mg alloy with submicrometer grain size. Acta Mater 1996;44(11):461–4629.

[59] Garibaldi M, Ashcroft I, Hillier N, Harmon SAC, Hague R. Relationship between laser energy input, microstructures and magnetic properties of selective laser melted Fe-6.9%wt Si soft magnets. Mater Charact Sep. 2018;143:144–51. https://doi.org/10.1016/j.matchar.2018.01.016.

[60] Garibaldi M, Ashcroft I, Lemke JN, Simonelli M, Hague R. Effect of annealing on the microstructure and magnetic properties of soft magnetic Fe-Si produced via laser additive manufacturing. Scripta Mater Jan. 2018;142:121–5. https://doi.org/10.1016/j.scriptamat.2017.08.042.

[61] Chikazumi S, Charap SH. Physics of magnetism. In: Pre... English ed./. New York: Wiley; 1964.

[62] Zanni M, Ceschini L, Fortunato A, Valli G, Del Bianco L, Spizzo F. Relationship between microstructure, mechanical and magnetic properties of pure iron produced by laser powder bed fusion (L-PBF) in the as-built and stress relieved conditions. Progress in Additive Manufacturing Dec. 2022;7(6):1195–212. https://doi.org/10.1007/s40964-022-00294-7.

[63] Cullity BD, Graham CD. Introduction to magnetic materials. second ed. Hoboken, NJ: John Wiley & Sons; 2009.